

1 **Mechanical properties of quartz sand and gypsum powder (plaster) mixtures:**  
2 **implications for laboratory model analogues for the Earth's upper crust**

3 **Sam Poppe**<sup>1,2\*</sup>, Eoghan P. Holohan<sup>3</sup>, Michael Rudolf<sup>4</sup>, Matthias Rosenau<sup>4</sup>, Olivier Galland<sup>5</sup>,  
4 Audray Delcamp<sup>1</sup>, Matthieu Kervyn<sup>1</sup>

5 1 Physical Geography, Department of Geography, Vrije Universiteit Brussel, Brussels,  
6 Belgium

7 2 now at Laboratoire G-Time, Department of Geoscience, the Environment and Society,  
8 Université Libre de Bruxelles, Brussels, Belgium

9 3 UCD School of Earth Sciences, University College of Dublin, Dublin 4, Ireland

10 4 Helmholtz Centre Potsdam - GFZ German Research Centre for Geosciences, Potsdam,  
11 Germany

12 5 Physics of Geological Processes, The Njord Center, University of Oslo, Oslo, Norway

13

14 **\*Corresponding author:** sam.poppe@ulb.be; sam35poppe@gmail.com

15

16

17

18 Please feel free to contact the authors, we welcome feedback. This manuscript has been  
19 published in TECTONOPHYSICS. The final version of this manuscript is available via the  
20 'Peer-reviewed publication DOI' link on the right-hand side of this webpage.

21

Please reference as:

22 Poppe, S., Holohan, E.P., Rudolf, M., Rosenau, M., Galland, O., Delcamp, A. and Kervyn,  
23 M., 2021. Mechanical properties of quartz sand and gypsum powder (plaster) mixtures:  
24 Implications for laboratory model analogues for the Earth's upper crust. *Tectonophysics*, 814,  
25 228976, <https://doi.org/10.1016/j.tecto.2021.228976>

26 **Title:**

27 **Mechanical properties of quartz sand and gypsum powder (plaster) mixtures:**  
28 **implications for laboratory model analogues for the Earth's upper crust**

29

30 **Authors:**

31 **Sam Poppe**<sup>1,2\*</sup>, Eoghan P. Holohan<sup>3</sup>, Michael Rudolf<sup>4</sup>, Matthias Rosenau<sup>4</sup>, Olivier Galland<sup>5</sup>,  
32 Audray Delcamp<sup>1</sup>, Matthieu Kervyn<sup>1</sup>

33 1 Physical Geography, Department of Geography, Vrije Universiteit Brussel, Brussels,  
34 Belgium

35 2 now at Laboratoire G-Time, Department of Geoscience, the Environment and Society,  
36 Université Libre de Bruxelles, Brussels, Belgium

37 3 UCD School of Earth Sciences, University College of Dublin, Dublin 4, Ireland

38 4 Helmholtz Centre Potsdam - GFZ German Research Centre for Geosciences, Potsdam,  
39 Germany

40 5 Physics of Geological Processes, The Njord Center, University of Oslo, Oslo, Norway

41

42 **\*Corresponding author:** sam.poppe@ulb.be; sam35poppe@gmail.com

43

44 **Highlights**

- 45 - Density, tensile strength, shear strength of sand-plaster mixtures quantified
- 46 - Cohesion and friction coefficients from Coulomb and Griffith failure criteria.
- 47 - Sensitivity to emplacement technique and ambient humidity.
- 48 - Brittle to plastic behaviour depending on plaster content and applied normal load.
- 49 - Tensile strength of sand-plaster mixtures as a scalable experimental parameter.

50 **Abstract**

51 Granular materials are a useful analogue for the Earth's crust in laboratory models of  
52 deformation. Constraining their mechanical properties is critical for such model's scaling and  
53 interpretation. Much information exists about monomineralic granular materials, such as  
54 quartz sand, but the mechanical characteristics of bimineralic mixtures, such as commonly-  
55 used quartz sand mixed with gypsum powder (i.e. plaster), are largely unconstrained. We used  
56 several mechanical tests (density, tensile, extension, shear) to constrain the failure envelope of  
57 various sand-plaster mixtures. We then fitted linear Coulomb and parabolic Griffith failure  
58 criteria to obtain cohesions and friction coefficients. Tests of the effects of emplacement  
59 technique, compaction and humidity demonstrated that the most reproducible rheology is  
60 given by oven-drying, pouring and mechanically compacting sand-plaster mixtures into their  
61 experimentation container. As plaster content increases, the tensile strength of dry sand-  
62 plaster mixtures increases from near zero (pure quartz sand) to  $166\pm 24$  Pa (pure plaster). The  
63 cohesion increases from near zero to  $250\pm 21$  Pa. The friction coefficient varies from  
64  $0.54\pm 0.08$  (sand) to  $0.96\pm 0.08$  (20 weight% plaster). The mechanical behaviour of the  
65 resulting mixtures shifts at 20-35 weight% plaster from brittle Coulomb failure along a linear  
66 failure criterion, to more complex brittle-plastic Coulomb-Griffith failure along a non-linear  
67 failure criterion. With increasing plaster content, the brittle-plastic transition occurs at  
68 decreasing depth within a pile of sand-plaster mixture. We infer that the identified transitions  
69 in mechanical behaviour with increasing plaster content relate to (1) increasing porosities, (2)  
70 increasing grain size distributions, and (3) a decrease in sand-sand grain contacts and  
71 corresponding increase in contacts of anisotropic gypsum-gypsum grains. The presented  
72 characterisation enables a more quantitative scaling of the mechanical behaviour of sand-  
73 plaster mixtures, including their tensile strength. Sand-plaster mixtures can thereby  
74 realistically simulate brittle-plastic properties of the Earth's crust in scaled laboratory models.

75

76 **Keywords:**

77 Laboratory modelling; Analogue materials; Quartz sand; Gypsum powder; Mechanical  
78 properties; Tensile strength; Shear strength; Cohesion; Friction coefficient

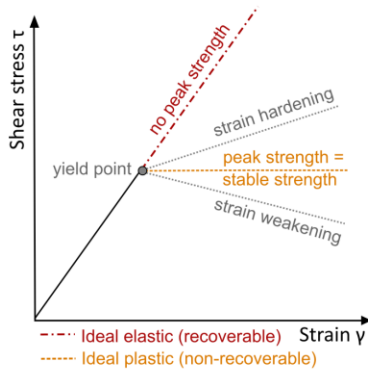
79

80 **1. Introduction**

81 The Earth's crust is a complex set of geological layers and structures, exhibiting a wide range  
 82 of physical and mechanical properties. Properties such as rock density, porosity, tensile  
 83 strength, shear strength, cohesion and internal friction control or relate to deformation of the  
 84 crust during geological processes (Graveleau et al., 2012; Hubbert, 1951, e.g. 1937; Labuz et  
 85 al., 2018). The mechanical response of rocks to a stress applied externally to the studied  
 86 volume can take several idealised forms. For an ideal, linearly elastic material, the  
 87 relationship between stress and strain follows a recoverable sloped linear trajectory, and the  
 88 material resumes its initial geometrical state after the stress is removed (Figure 1A) (Jaeger et  
 89 al., 2007). For an ideal plastic material, the relationship between stress and strain is initially  
 90 similar to an elastic material, but at a certain shear stress threshold the plastic material  
 91 undergoes 'yielding', after which the strain is non-recoverable (Jaeger et al., 2007). The strain  
 92 vs. stress curve then becomes horizontal and defines a stable strength value (Figure 1A). Such  
 93 idealised behaviours are widely used concepts for models of tectonic and magmatic crustal  
 94 deformation (e.g. Scheibert et al., 2017; Vachon and Hieronymus, 2017).

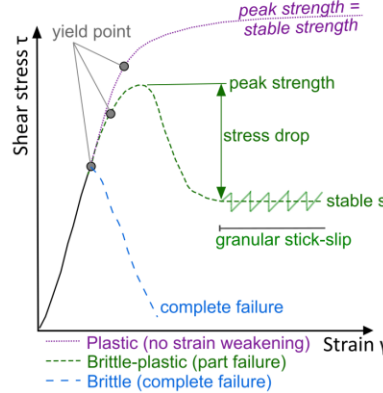
95

96 **A Ideal material**

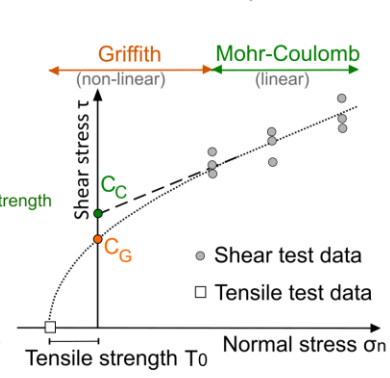


104 **Figure 1** – **A** Shear stress ( $\tau$ ) in an ideal Coulomb material that is subjected to an angular shear ( $\gamma$ ) increases  
 105 linearly until failure occurs and a constant peak strength is reached; **B** Shear stress in natural rocks under low  
 106 confining stress increases until the yield point is reached after which either shear stress increases towards a stable  
 107 strength in the plastic regime, or until a peak strength where failure occurs and shear stress again decreases  
 108 towards a lower stable strength in the brittle-plastic regime (the difference is the stress drop), or after which  
 109 shear stress decreases until complete failure in the brittle regime; **C** Shear test results from samples subjected to  
 110 different confining normal loads ( $\sigma_n$ ), combined with tensile strength ( $T_0$ ) obtained from tensile tests together  
 111 define the two-dimensional Mohr failure envelope of a material; the intercept with the vertical axis ( $\tau$ ) is the  
 112 material's cohesion and can be estimated using e.g. a linear Coulomb ( $C_C$ ) or non-linear Griffith ( $C_G$ ) failure  
 113 criterion (cfr. Jaeger et al. 2007).

96 **B Natural rocks**



96 **C Failure envelope**



114 Laboratory tests on natural rocks have shown a more complex behaviour (Byerlee, 1978;  
115 Jaeger et al., 2007). Upon or after ‘yielding’, a peak strength may be reached, after which the  
116 rock sample typically fails along a localised shear plane. The shear stress then decreases  
117 towards a lower, stable – or ‘residual’– strength (Figure 1B, green). The difference between  
118 the peak strength and stable strength is the so-called stress drop. The stable strength may  
119 gradually increase or decrease at continued shearing, referred to as strain hardening or strain  
120 weakening respectively (Figure 1B). Upon brittle failure, a sharp stress drop leads to an  
121 abrupt decrease in shear strength and – in the lab – can result in sample disintegration (Figure  
122 1B, blue). Brittle failure is typical for low lithostatic pressures in the upper part of the crust  
123 (Paterson and Wong, 2005).

124 With plastic deformation of natural rocks, in contrast, the stress drop is absent (Figure 1B,  
125 purple), and it typically occurs at higher lithostatic pressures (i.e. at greater depths in the  
126 crust) (Byerlee, 1968; Jaeger et al., 2007; Schöpfer et al., 2013). Plastic materials undergo no  
127 strain weakening and the shape of the failure envelope does not change with increasing  
128 deformation, i.e. the deformation is time-independent and non-recoverable. See Wang (2021)  
129 for further discussion of brittle-plastic terminology. The brittle-plastic transition describes the  
130 level in the crust above which rock deformation is brittle, and below which it is plastic.

131 These insights of rock mechanics have been used for decades in laboratory – or analogue –  
132 experiments to study deformation processes in the Earth’s crust, such as tectonic faulting (e.g.  
133 Dooley and Schreurs, 2012; Hubbert, 1937), seismo-tectonics (e.g. Reid, 1911; Rosenau et al.,  
134 2017), magma intrusion (e.g. Galland et al., 2018; Kavanagh et al., 2018b; Mastin and  
135 Pollard, 1988; Poppe et al., 2019) and gravitational collapse (e.g. Marti et al., 1994; Merle and  
136 Borgia, 1996). The selection of analogue materials is guided by the aim of obtaining physical  
137 similarity between the experiments and nature through dimensional analysis (Hubbert, 1937;  
138 Merle, 2015). Such considerations have favored the use of low-cohesive, frictional granular  
139 materials – dominantly sands (e.g. Cubas et al., 2013; Klinkmüller et al., 2016; Montanari et  
140 al., 2017; Roche et al., 2000; Schreurs et al., 2016, 2006), although another type of laboratory  
141 models use materials with simplified elastic or visco-elastic rheologies such as pigskin gelatin  
142 or laponite gel (e.g. Bertelsen et al., 2018; Kavanagh et al., 2018a; Rivalta et al., 2015 and  
143 references therein). Coulomb (1775) was the first to describe a linear relationship between  
144 normal load and shear stress at failure for granular media. Like rocks, sand is considered to  
145 deform largely according to a Mohr-Coulomb failure criterion (Figure 1C, green), with a  
146 realistic strain weakening behaviour controlling localisation of deformation into shear zones  
147 (Lohrmann et al., 2003; Ritter et al., 2016).

148 Studies using laboratory models traditionally focused on qualitative descriptions of structural  
149 geometries (e.g. Eisenstadt and Sims, 2005; Holohan et al., 2013; Roche et al., 2000).  
150 Recently, model deformation fields are routinely quantified by using advanced  
151 photogrammetry and image analysis techniques (e.g. Adam et al., 2005; Galland et al., 2016;  
152 Tortini et al., 2014) and most recently X-ray Computed Tomography (CT) (Adam et al., 2013;  
153 Holland et al., 2011; Kervyn et al., 2010; Poppe et al., 2019; Schreurs et al., 2003; Zwaan and  
154 Schreurs, 2017). Lately, such kinematic observations have been blended with both internal  
155 “in-situ” stress measurements (Moulas et al., 2019; Nieuwland et al., 2000; Seropian and Stix,  
156 2018) and constraints on externally applied forces (Cruz et al., 2010; Cubas et al., 2013;  
157 Herbert et al., 2015; Ritter et al., 2018b, 2018a; Souloumiac et al., 2012) to derive a  
158 quantitative dynamic picture of faulting or other deformation processes in laboratory models.  
159 Different emplacement techniques (sieving, pouring) yield sand packings of variable  
160 reproducibility, as demonstrated by mechanical tests (Lohrmann et al., 2003; Panien et al.,  
161 2006). Moreover, benchmarking experiments using different sands have demonstrated that  
162 variability in the granular characteristics (i.e. angularity, ellipticity) introduces uncertainties in  
163 quantified model outcomes (Schreurs et al. 2016). The evolution towards a more quantitative  
164 analysis of laboratory models requires quantified mechanical properties of granular  
165 analogues, the reduction of reproducibility uncertainty and better scaling of laboratory models  
166 to their natural prototypes (Gomes et al., 2006; Lohrmann et al., 2003; Montanari et al., 2017;  
167 Panien et al., 2006; Ritter et al., 2016).

168 Density, cohesion and friction coefficient are the three main parameters that have been used in  
169 dimensional analysis for scaling granular analogue materials. These properties can be  
170 obtained from a granular material by using mechanical tests, such as direct and ring shear  
171 tests (Abdelmalak et al., 2016; Galland et al., 2009; Merle, 2015; Montanari et al., 2017;  
172 Mourgues and Cobbold, 2003; Schellart, 2000; Zorn et al., 2020). Compared to sand – which  
173 is near-cohesionless –, more cohesive powders with finer grain sizes in the order of a few  $\mu\text{m}$ ,  
174 such as silica flour, crushed (feldspar) sand, alumina powder, ignimbrite powder, kaolin clay,  
175 diatomite powder, powder sugar, wheat flour and gypsum powder, can be used purely or  
176 mixed as a filler into coarser-grained sand to represent more complex crustal deformation  
177 (e.g. Galland et al., 2018, 2006; Grosse et al., 2020; Mathieu et al., 2008; Montanari et al.,  
178 2017; Reber et al., 2020; Schellart and Strak, 2016 and references therein). These powders are  
179 able to form both tensile fractures and shear fractures, and they may follow a non-linear  
180 Griffith-Mohr-Coulomb failure criterion (Figure 1C, orange), instead of a linear Coulomb  
181 failure criterion (Figure 1C, green) (Abdelmalak et al., 2016; van Gent et al., 2010).

182 Abdelmalak et al. (2016) showed that a combination of mechanical tests can make cohesion  
183 and friction coefficient tunable experimental variables for fine-grained materials of low-  
184 cohesion, low-friction grains mixed with high-cohesion, high-friction grains.

185 As example of fine-grained filler in sand, hemihydrate gypsum powder (i.e. plaster) has been  
186 used in laboratory models of volcano-tectonic processes, such as magma intrusion, dome  
187 building or gravitationally-driven deformation (Byrne et al., 2015, 2013; Donnadiou et al.,  
188 2001; Holohan et al., 2008; Kervyn et al., 2010; Merle and Lénat, 2003; Poppe et al., 2019,  
189 2015; Rincón et al., 2018; Roche et al., 2001; Zorn et al., 2020), and regional-tectonic  
190 processes, such as the evolution of normal fault zones in high-strength rocks (van Gent et al.,  
191 2010), near-surface gravitational instabilities, such as sinkhole collapse (Poppe et al., 2015)  
192 and landslides (Paguican et al., 2014; Shea and van Wyk de Vries, 2008). Apart from limited  
193 efforts (Donnadiou et al., 2001; Zorn et al., 2020), the physical and mechanical properties of  
194 often-used sand-plaster mixtures have not been systematically investigated, even though they  
195 might have significant implications on the interpretation of experimental results.

196 This study quantifies the mechanical behaviour of quartz sand mixed with gypsum powder at  
197 different weight ratios, by evaluating different mechanical testing methods. We first provide  
198 the context for the scaling of mechanical properties of analogue granular materials. We test  
199 the influence of the emplacement technique – pouring, sieving and compaction – on bulk  
200 density and estimate the material porosities. We also test the effect of ambient humidity. By  
201 using tensile tests, extensional tests, direct shear tests and ring shear tests, we constrain failure  
202 envelopes for each of the end-member sand and plaster materials and mixtures thereof. By  
203 assessing the goodness-of-fit of linear Coulomb versus parabolic Griffith failure criteria to the  
204 failure data, we then estimate the cohesion and friction coefficient. Our results enable a better  
205 understanding of modelling outcomes involving sand and plaster and their mixtures, and  
206 allow more realistic dynamic scaling of laboratory experiments using such materials.

207

## 208 **2. Scaling of the mechanical properties of granular materials**

209 The concept of scaling and dimensional analysis implies two successive steps: (1) identifying  
210 the dimensionless parameters that govern the modelled physical system, and (2) the  
211 geometrical, mechanical and dynamical equivalence – i.e. similarity – of laboratory models to  
212 their natural counterparts (Barenblatt, 2003; Gibbings, 2011; Hubbert, 1937). Abdelmalak et  
213 al. (2016), Merle (2015) and Reber et al. (2020) summarise how this equivalence can be  
214 reached for granular materials.

215 Dynamic similarity is classically discussed by assuming that a Coulomb failure criterion is  
216 representative of material failure in both model (*m*) and a natural prototype (*g*). The internal  
217 friction coefficient  $\mu$  is a direct dimensionless parameter. Dynamic similarity implies that the  
218 friction coefficient of the model material must be equal to that in geological natural systems:

$$219 \quad (1) \mu_m = \mu_g$$

220 The cohesion *C* is combined with density  $\rho$ , gravitational acceleration *g*, and depth or length *h*  
221 (Hubbert, 1945; Merle, 2015) in the dimensionless parameter:

$$222 \quad (2) \Pi = \frac{\rho \times g \times h}{C},$$

223 This parameter quantifies the balance between the gravitational forces and the cohesive  
224 forces; the system will be gravity-dominated if  $\Pi \gg 1$  and cohesion-dominated if  $\Pi \ll 1$ . In  
225 addition, the model material cohesion  $C_m$  required for a model that is subjected to the natural  
226 gravity field is calculated by rearranging equation (2):

$$227 \quad (3) C_m = \frac{C_g}{\rho_g \times h_g} \rho_m \times h_m,$$

228 Accordingly, the model cohesion dictates the length scale  $h_g$  of the model with respect to the  
229 natural prototype. Different scales of observation, e.g. basin-scale vs. lithosphere scale,  
230 therefore necessitate different model cohesions (Abdelmalak et al., 2016). The length scale  $h^*$   
231 represents the dimensionless scale ratio between model and nature and equals  $h_m/h_g$  (Table 1).  
232 In laboratory models of lithosphere-scale processes, one centimeter typically represents 10  
233 km, translating into  $l^* \approx 10^{-6}$  (e.g. Davy and Cobbold 1991), while in those of basin-scale  
234 processes, one centimeter most typically represents 100 to 1000 meters, translating into  $l^* =$   
235  $10^{-4}$ - $10^{-5}$  (e.g. Dooley and Schreurs, 2012; Galland et al., 2018; Merle, 2015). Bulk densities  
236 of most natural crustal rocks range between 2200 and 3000  $\text{kg.m}^{-3}$ , while analogue granular  
237 material bulk densities range between 1200 and 1800  $\text{kg.m}^{-3}$ . This leads to model:nature  
238 density ratios  $\rho^*$  of 0.4-0.8. Cohesions of natural rocks range broadly between  $10^6$  and  $10^8$  Pa  
239 (e.g. Galland et al., 2018; Schellart, 2000; Schultz, 1996; Voight and Elsworth, 1997).

240 For lithosphere-scale processes,  $\Pi$  values then range between 2 and 300, and so cohesions of  
241 model rocks should be considerably low, between 0.5 and 80 Pa. This is the case for pure  
242 silica sand (Klinkmüller et al., 2016; Schellart, 2000). For basin-scale or volcano-scale  
243 processes,  $\Pi$  values lie an order of magnitude lower, between 0.2 and 30, and cohesions of  
244 model materials should have a range between 40 and 800 Pa. Granular materials with higher  
245 cohesion compared to sand are thus needed, by using fine-grained powders or fillers in  
246 coarse-grained sand.

247



248 **Table 1:** Scaling parameters and dimensionless equation used to compare experiments to nature;  
 249 natural values from (Galland et al., 2014; Merle, 2015; Schultz, 1996).

Parameter	Symbol and Unit	Model (m)	Nature(g)	Ratio*
Gravitational acceleration	$g$ (m.s <sup>-2</sup> )	~9.81	~ 9.81	~1
Overburden height	$h$ (m)	$1 \times 10^{-2}$	$1 \times 10^1 - 15 \times 10^3$	$10^{-4} - 10^{-6}$
Density	$\rho$ (kg.m <sup>-3</sup> )	1200-1800	2200-3000	0.4-0.8
Cohesion	$C$ (Pa)	0.5-800	$10^6 - 10^8$	$10^{-4} - 10^{-8}$
Internal friction angle	$\Phi$ (°)	25-45	25-45	~1
Internal friction coefficient	$\mu$ (radians)	0.43-0.79	0.43-0.79	~1
Gravitational stress:cohesion	$\square = \rho gh/C$	0.2-300	$0.015 \times 10^{-4} - 4 \times 10^3$	

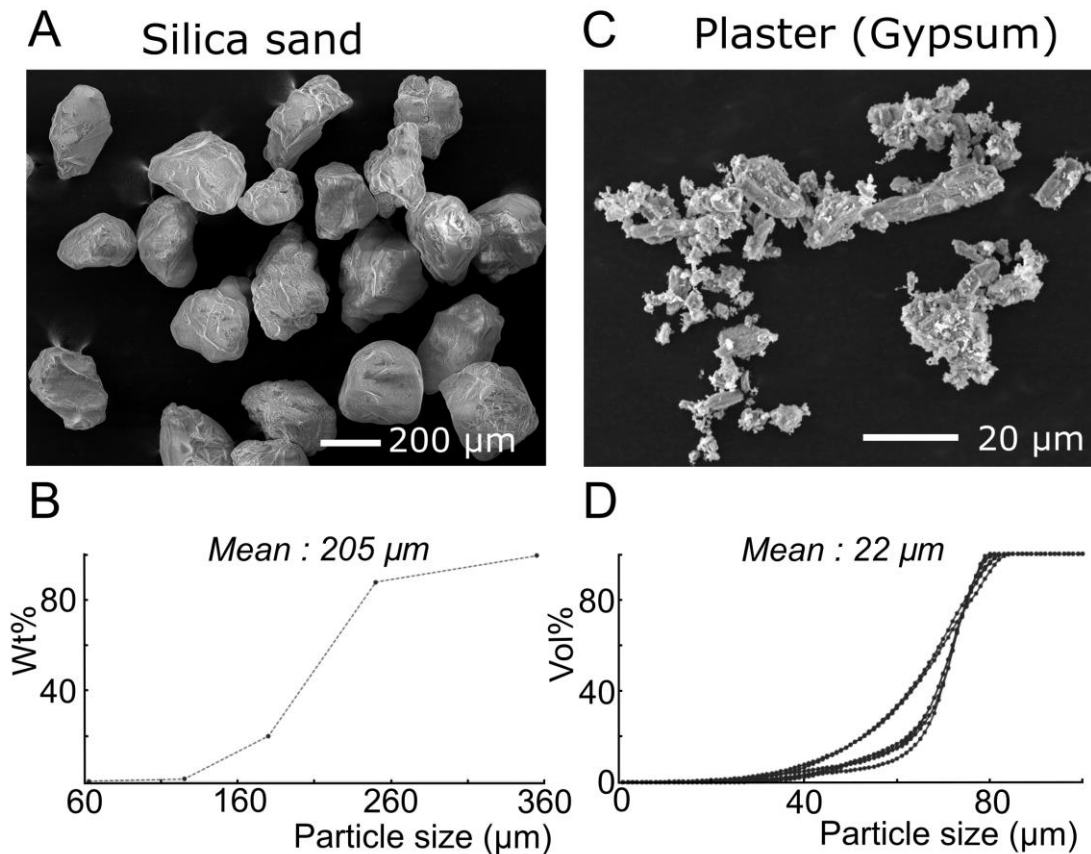
250

### 251 3. Materials and Methods

#### 252 3.1 Materials

253 We tested mixtures of dry sand and plaster. The sand is 99,8% chemically pure silica sand  
 254 MAM1ST-300 (SiO<sub>2</sub>; Sibelco, Mol, Belgium). Scanning Electron Microscope (SEM) images,  
 255 carried out at Vrije Universiteit Brussel, show that the grains are subangular to poorly  
 256 rounded (Figure 2A). The grain size is unimodal, with a mean ~205  $\mu\text{m}$  (Figure 2B). The  
 257 plaster is air-dried hemi-hydrate gypsum powder with the brand name Goldband (CaSO<sub>4</sub>.1/2  
 258 H<sub>2</sub>O; Knauf). SEM images show the grains are tabular to plate-shaped, and clustered (Figure  
 259 2C). Grain size measurements in water in a laser diffractometer without scintillation at Vrije  
 260 Universiteit Brussel showed that the grain size distribution is unimodal, with a mean ~22  $\mu\text{m}$   
 261 (Figure 2D). This combines both 1-10  $\mu\text{m}$ -sized individual crystals and 10-80  $\mu\text{m}$ -sized  
 262 clusters. The crystal hardness of quartz is 7 on the scale of Mohs, while that of gypsum  
 263 crystals is 4.

264 The sand and plaster were mixed at 0, 5, 10, 20, 35, 50, 70 and 100 weight percent (wt%) of  
 265 plaster. The quartz sand and gypsum plaster end-member materials and their mixtures are  
 266 hereafter referred to as 'samples'. Ambient air temperature was registered in all laboratory  
 267 environments to be 18-25°C.



268

269 **Figure 2** – **A.** Scanning Electron Microscope (SEM) image of MAM1ST-300 silica sand grains shows  
 270 moderately rounded grain shapes and a unimodal grain size; **B.** Cumulative particle size measurements show the  
 271 silica sand used in this study has a mean particle size of 205  $\mu\text{m}$  (Sibelco); **C.** SEM image of Knauf gypsum  
 272 powder – i.e. plaster - used in this study shows micrometer-sized, tabular and blocky crystals often in clusters of  
 273 several tens of  $\mu\text{m}$ ; **D.** Cumulative particle size measurements show that the mean plaster particle size is about  
 274 22  $\mu\text{m}$  but clusters sizes are up to 80  $\mu\text{m}$ .

275

## 276 3.2 Methods

### 277 3.2.1 Bulk density estimates and effects of emplacement method

278 The effects of three emplacement methods were assessed: (1) pouring, (2) sieving, and (3)  
 279 pouring and compaction. The first two methods were assessed by systematically measuring  
 280 the bulk density  $\rho$  of sand-plaster mixtures with 0, 10, 20, 50 or 100 wt%. plaster in ring shear  
 281 tests (see Section 3.2.3). The air-dried granular materials were placed into a ring-shaped shear  
 282 cell, either by sieving through a 400  $\mu\text{m}$  mesh, or by pouring from an open pitcher. The shear  
 283 cell is 4 cm high,  $1.10^{-3}$   $\text{m}^3$  (1 liter) in volume and of a mass of 2186.5 g. The samples were  
 284 emplaced from  $\sim 20$  cm height, which was previously found to be the most efficient height for  
 285 obtaining a most compact quartz sand packing (Lohrmann et al., 2003). Surplus material was

286 scraped off the cell top manually and the emplaced sample mass was then obtained by  
287 weighing the filled test cell on a balance.

288 The third emplacement method, and the effects of humidity, were examined through a second  
289 set of identical mixtures that were oven-dried for 24 hours at 90°C, poured in the shear cell  
290 from ~20 cm height and compacted by preloading with a normal load of 20000 Pa on the ring  
291 shear tester. The ring shear test procedure includes the estimation of material density before  
292 and during the test, which provided a means of assessing the effect of material compaction  
293 during deformation (see Section 3.2.3).

294

### 295 **3.2.2 Porosity estimates**

296 The bulk porosity  $\phi$  of each granular material was estimated through the equation:

$$297 (4) \phi = (V_s - ((M_s \cdot F_q) / \rho_q) + ((M_s \cdot F_p) / \rho_p)) / V_s$$

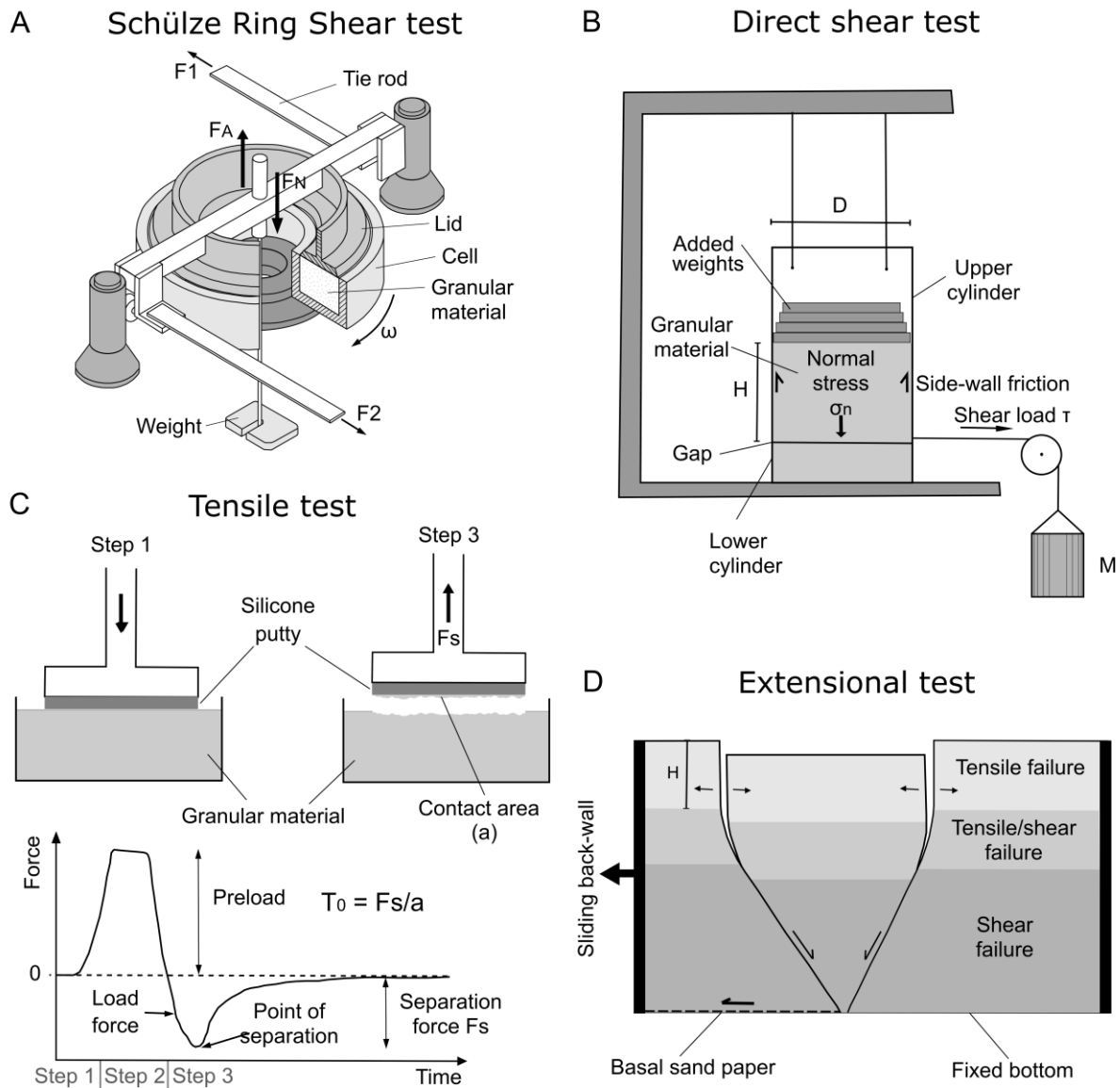
298 Here,  $F_q$  and  $F_p$  are the known bulk fractions of quartz sand and gypsum powder, respectively.  
299  $V_s$  is the sample bulk volume and  $M_s$  is the sample bulk mass. The individual crystal density  
300 of quartz  $\rho_q$  is taken to be 2655 kg.m<sup>-3</sup> and that of hemihydrate gypsum  $\rho_p$  is taken to be 2730  
301 kg.m<sup>-3</sup> (van Gent et al., 2010).

302

### 303 **3.2.3 Ring shear tests**

304 We generally followed the ring shear test protocol for measuring internal friction with the  
305 RST01.pc as described in Klinkmüller et al. (2016). The shear cell containing the sample was  
306 placed on the ring shear tester (Figure 3A) and the lid was lowered into the sample surface. A  
307 normal load was then applied by the lid to the air-dried poured or sieved sample under rest,  
308 that varied in separate test runs from 500, 1,000, 5,000, 10,000, 15,000 to 20,000 Pa. For  
309 comparison with direct shear test data, oven-dried samples were poured and then compacted  
310 in the ring shear cell by pre-loading with a normal load of 20,000 Pa for 5 seconds. Then, the  
311 normal load was returned to 250, 500, 1,000, 2,000 or 5,000 Pa respectively in separate test  
312 runs.

313 The cell was then rotated clockwise at a constant angular velocity of 4.4°.min<sup>-1</sup>, or 6 mm.min<sup>-1</sup>  
314 <sup>1</sup> (with respect to the median line of the sample-contained ring of the shear cell) during 300  
315 seconds (or 30 mm of shear). A set of 5-mm deep, vertical radial blades on the lid caused  
316 localisation of shear inside the sample material and prevented shear at the interface between  
317 the sample and the cell lid. During the test all signals from sensors (normal and shear load, lid  
318 position and velocity) were recorded at 100 Hz and then down-sampled to 10 Hz to smooth  
319 high-frequency noise.



320

321 **Figure 3** – Laboratory set-ups used for testing the physical properties of granular materials. **A.** Schülze ring  
 322 shear tester (RST). The sample is placed in an annular cell and on top of the sample a lid is suspended to which a  
 323 normal load is applied. During a test run the sample-bearing cell is rotated and tie rods measure the shear stress  
 324 ( $F_1$ ,  $F_2$ ) undergone by the lid. **B.** Hubert-type direct shear tester apparatus, in which a sample is placed in a  
 325 cylinder consisting of an upper half suspended above a stable lower half. A shear load  $M$  is applied to the upper  
 326 cylinder and is incrementally increased until sample failure occurs. Tests are repeated with constant sample  
 327 height  $H$  but increasing normal loads by adding weights. **C.** Tensile test where the tensile strength of a  
 328 compacted granular sample is obtained through a 3-step procedure in which a silicone pad is preloaded on the  
 329 top of a granular sample and subsequently retracted until sample failure occurs at a measured separation force.  
 330 **D.** Extensional test in which a compacted granular sample is extended horizontally until failure occurs by  
 331 retracting a moving wall. The height  $H$  of the vertical upper part in the tensile failure domain of the induced  
 332 fractures is a measure for the tensile strength of the material.

333

334 The registered shear stress curve is typical for granular materials (Figure 1B, green) and  
335 consists of three parts (Lohrmann et al., 2003; Panien et al., 2006): (1) a peak shear strength  
336 (i.e. static failure) that is reached shortly after test initiation, (2) a stress drop then reflects  
337 localisation of shear into a shear zone; (3) a stable plateau is reached representing the steady  
338 state stable shear strength; (4) after a short reversal of shear cell rotation direction to return  
339 shear stress to zero, shearing anew in a clockwise direction returns the shear curve to a  
340 dynamic shear strength which represents shear zone reactivation.

341 For each normal load, tests were repeated three times, amounting to 18 tests for each material  
342 in total. Peak shear strengths were picked manually or automatically (Rudolf and Warsitzka,  
343 2019; Warsitzka et al., 2019). Stable and dynamic shear strengths are not discussed further  
344 here, but they are available in the accompanying data publication (Poppe et al., 2021).

345 During shearing, vertical lid movement is measured as a proxy for sample decompaction  
346 (positive) or compaction (negative). This measurement allowed us to study the effect of  
347 sample decompaction/compaction, and thus density variations, on sample frictional  
348 properties.

349 An additional velocity stepping test was carried out on a 90 wt% sand – 10 wt% plaster  
350 mixture to assess the dependency of measured shear strengths on the shear rate, by decreasing  
351 the shear rate after reaching the steady state plateau incrementally from 5 mm.s<sup>-1</sup> to 2.5, 1,  
352 0.5, 0.1 and 0.05 mm.min<sup>-1</sup>.

353

#### 354 **3.2.4 Humidity tests**

355 To estimate the humidity content, one air-dried sample of a mass of ~400g of each sand,  
356 plaster, and sand-plaster mixtures containing 5, 10, 20, 35, 50 and 70 wt% plaster, all stored  
357 previously in their original packaging at room temperature and ambient air humidity, were  
358 weighed on a precision balance (precision = 0.01g). Then, the samples were placed in open  
359 containers in an oven at a temperature of 90°C and weighed again after 24, 48 and 72 hours of  
360 oven-drying. The drying process evaporated the sample's moisture, and the loss of sample  
361 mass yielded a weight percentage (wt%) of humidity loss. Furthermore, to constrain the effect  
362 of humidity on the mechanical properties of 100 wt% plaster, we carried out direct shear tests,  
363 tensile and extensional tests both on oven-dried plaster and on air-dried plaster.

364

#### 365 **3.2.5 Direct shear tests**

366 Pressures of <500 Pa are typical in sand-box experiments with a few centimeters of material  
367 height (depending on material density - cf. equation 2). Because standard ring shear tests at

368 normal loads of  $< 500$  Pa are possibly subject to bias (Ritter et al., 2016), we performed  
369 Hubert-type direct shear tests at normal loads of  $\sim 100$  to  $\sim 1200$  Pa. The Hubert-type shear  
370 apparatus consisted of an upper PVC cylinder suspended above a fixed lower PVC cylinder,  
371 with a cardboard ring maintaining a gap of  $< 1$  mm in between both cylinders (Figure 3B).  
372 To avoid humidity effects on material properties, samples were first oven-dried at  $90^\circ\text{C}$  for at  
373 least 24 hours, left to cool in a sealed container, weighed on a precision balance and poured in  
374 the cylinders of the shear apparatus. A lid was placed on top of the sample, and by manual  
375 tapping from above on the lid, the sample was compacted down until a height  $H$  of 2.5 cm  
376 above the gap between both cylinders to obtain the density pre-determined for that material  
377 ( $\rho_{\text{Compacted}}$  in Table 2). The mass of material within the upper cylinder under gravity  
378 represented an initial normal load on the horizontal plane passing between the cylinders. Up  
379 to four weights could be added on top of the sample, to give a range of five normal loads. The  
380 normal stress  $\sigma_n$  acting on the horizontal plane between the cylinders is obtained by dividing  
381 normal load by the circular area of the plane. After sample emplacement, compaction and  
382 vertical loading, the cardboard ring between both cylinders was carefully removed without  
383 disturbing the sample. To obtain the shear strength  $\tau$ , a shear load was applied to the upper  
384 cylinder by pouring sand in a small container connected to the cylinder via a pulley (Figure  
385 3B). This load was increased until an initial sample failure was detected by visual inspection  
386 at the gap between both cylinders. The applied mass  $M$  causing shear failure was then  
387 constrained by weighing. From this, the gravitational acceleration  $g$ , and the circular shear  
388 plane area  $A$  (i.e. cylinder section), the sample's shear strength (i.e. the critical shear stress  
389 acting on the shear plane) was calculated according to the equation:

390 (5)  $\tau = gM/A$

391 This test was repeated three times for each of the five normal loads to ensure minimum  
392 reproducibility. Thus, a total of 15 measurements were made for each mixture and end-  
393 member granular material. In cases where the range of the obtained measurement values was  
394 large, additional runs were carried out. The average shear strength value at each normal load  
395 was used to construct failure envelopes in shear stress  $\sigma_s$  vs. normal stress  $\sigma_n$  diagrams,  
396 following correction of the normal stress for the so-called silo effect.

397 The 'silo effect' or 'Janssen effect' is a reduction in the normal load on the shear plane due to  
398 friction on the wall of the upper cylinder (Jansen, 1895; Mourgues and Cobbold, 2003). This  
399 can be corrected empirically. The upper cylinder of the Hubbert-type shear apparatus was  
400 suspended above a precision balance. A cardboard ring maintained a gap of  $< 1$  mm between  
401 the cylinder and the balance. A sample was then poured and compacted in the suspended

402 cylinder to obtain the same densities as used in the direct shear tests (Table 2). The cardboard  
403 ring was then removed. The mass then registered by the balance was the effective normal load  
404 exerted on the failure plane in the direct shear tests. These normal load measurements were  
405 repeated at least three times for each of the five normal loads in the direct shear tests, and the  
406 average ‘corrected normal load’ was used instead of the theoretical normal load to construct  
407 failure envelopes.

408

### 409 **3.2.6 Tensile tests**

410 The tensile strength  $T_0$  of oven-dried sand, plaster and sand-plaster mixtures containing 5, 10,  
411 20, 35, 50 and 70 wt% plaster, and air-dried plaster was measured at Le Mans Université,  
412 France, following the method of Schweiger and Zimmerman (1999). Each material was  
413 poured into a container of 108 cm<sup>3</sup> in volume and with a square-shaped area of 6x6 cm<sup>2</sup>. It  
414 was then compacted by manually tapping a cover from above to obtain the required density  
415 (Figure 3B). A pad of the silicone polymer polydimethylsiloxane (PDMS) with a viscosity of  
416  $\sim 10^4$  Pa.s (Poppe et al., 2019) was attached to the bottom of a square-shaped load cell  
417 measuring 4x4 cm<sup>2</sup>, which was mounted on an EZ-SX tension apparatus.

418 The tensile strength test consisted of three steps (Figure 3C). In step 1, the sample was  
419 vertically preloaded by the load cell for five seconds to allow the silicone to adhere to the  
420 sample surface. In step 2, the loading was reduced until the tension force sensor measured 0  
421 N. In step 3, an increasing vertical tensional force was exerted on the granular material by  
422 moving the silicone pad upwards at a constant displacement rate until a peak tension force  $F_t$   
423 was reached at failure. A photograph of the post-test silicone pad was orthorectified in  
424 ArcGIS software (ESRI), where the area of separated granular material  $A_s$  was traced and  
425 quantified. The tensile strength  $T_0$  was then obtained through the equation:

$$426 \quad (6) \quad T_0 = F_t/A_s$$

427 Tensile strength tests were reproduced ten times for the sand and plaster end-members and  
428 each sand-plaster mixture.

429

### 430 **3.2.7 Extension tests**

431 On the assumption that the failure envelope of a material is non-linear at negative normal  
432 loads and at small positive normal loads, the cohesion of granular materials can be estimated  
433 by combining the tensile strength  $T_0$  with a vertical cliff height  $H$  obtained from extensional  
434 tests (Abdelmalak et al., 2016).  $H$  was measured at the Vrije Universiteit Brussel, Belgium, in  
435 an extensional apparatus that consists of a box with three fixed glass walls and one moving

436 wall connected to a computer-controlled piston (Figure 3D). Attached to the moving wall was  
437 sandpaper that covered half of the box bottom length.

438 A weighed amount of oven-dried sand, plaster or sand-plaster mixtures containing 5, 10, 20,  
439 35, 50 and 70 wt% plaster, or air-dried plaster was poured in the box. Sample compaction to a  
440 vertical height of 10 cm and the required density (see Table 2) was obtained by manual  
441 tapping on a lid from above. By moving the wall laterally outwards at a constant rate of 10  
442 cm/hr, the attached sandpaper imposed a velocity discontinuity to the base of the sample pack,  
443 which extended until two or more fractures developed, forming a graben-like structure. At  
444 and just below the surface, each fracture is vertical and opening mode in the tensile failure  
445 domain; with depth the fracture becomes inclined and transitions to shear mode in the shear  
446 failure domain (Figure 3D). We measured the height H of the opening-mode shallow part of  
447 the fractures.

448

## 449 **4. Results**

### 450 **4.1 Effects of emplacement method**

451 We observed clear effects of the method of emplacement of sand-plaster mixtures – i.e.  
452 sieving, pouring or pouring + compaction – on the heterogeneity, density and porosity of the  
453 sample material.

454

#### 455 **4.1.1 Material heterogeneity**

456 The spatial grainsize distribution of a sand-plaster mixture, and thus of mineralogy, is  
457 strongly affected by the emplacement method. Pouring a mixture quasi-instantaneously  
458 maintained a homogeneous sand and plaster distribution as visually observed in Figure 4A.  
459 Sieving the mixture, however, resulted in heterogeneous grain-size and mineralogical  
460 distribution as the sand and plaster separated into thin layers (Figure 4A).

461

#### 462 **4.1.2 Material density**

463 The pre-test bulk densities show systematic variation depending on the emplacement method  
464 and sand-plaster mixing ratios (Figure 4B; Table 2). Firstly, the mean density of quartz sand  
465 is significantly higher when sieved ( $1410 \pm 5 \text{ kg m}^{-3}$ ) than poured ( $1235 \pm 7 \text{ kg m}^{-3}$ ) ( $\alpha =$   
466  $0.050$ ;  $p = 1.69 \times 10^{-25}$ ;  $t\text{-statistic} = -127.61$ ;  $t\text{-critical} = 2.12$ ), whereas the density of plaster is  
467 significantly lower when sieved ( $564 \pm 6 \text{ kg m}^{-3}$ ) than poured ( $636 \pm 11 \text{ kg m}^{-3}$ ) ( $\alpha = 0.050$ ;  $p$   
468  $= 4.40 \times 10^{-13}$ ;  $t\text{-statistic} = 21.03$ ;  $t\text{-critical} = 2.12$ ). At a 50:50 wt% sand:plaster ratio, the



469 density of sieved ( $899 \pm 7 \text{ kg m}^{-3}$ ) and poured ( $906 \pm 9 \text{ kg m}^{-3}$ ) samples is not significantly  
470 different ( $\alpha = 0.050$ ;  $p = 6.67 \times 10^{-2}$ ; t-statistic = 1.97; t-critical = 2.12).

471 Secondly, pouring+compaction produced higher bulk densities than either sieving or pouring.  
472 Compaction increased the bulk density of plaster to  $900 \text{ kg m}^{-3}$  regardless of whether done by  
473 pre-loading (RST) or tapping (DST). Compaction by tapping more effectively increased the  
474 bulk density for sand-rich mixtures (i.e. <35 wt% plaster) and produced a bulk density of  
475  $1700 \text{ kg m}^{-3}$  for the sand end-member; this is approximately double that of plaster (Figure 4B;  
476 Table 2).

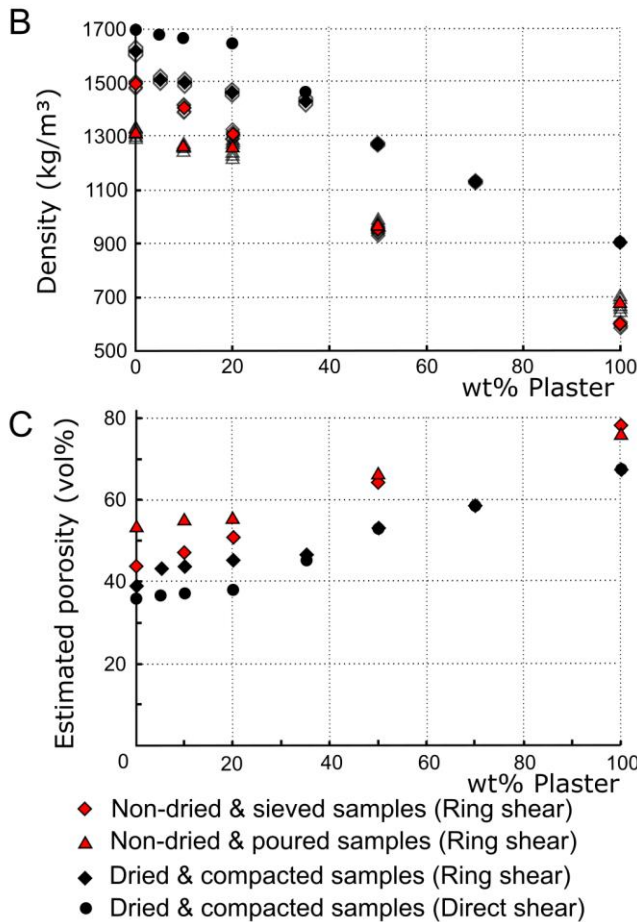
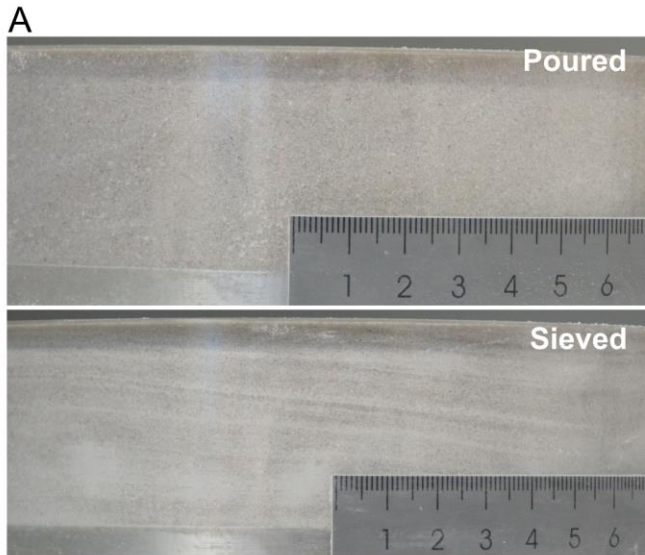
477 Thirdly, whether poured, sieved or poured+compacted, the bulk density of a sand-plaster  
478 mixture systematically decreases with increased plaster content. This decrease is not linear –  
479 bulk density decreases more rapidly for both the poured and the poured+compacted samples  
480 after about 20 - 35 wt% plaster.

481

#### 482 **4.1.3 Material porosity**

483 The estimated bulk porosity of the samples relates inversely to the bulk density (Figure 4C;  
484 Table 2). Depending on the emplacement technique, the inferred porosity of quartz sand was  
485 varied between 36-54 vol%, whereas that of plaster varied between 67-78 vol%. In mixtures  
486 of these end-members, the porosity increased systematically, but non-linearly, with increasing  
487 plaster content by weight.

488



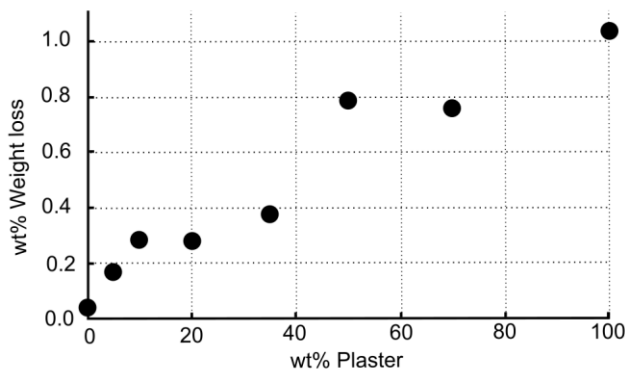
489 **Figure 4** – Effect of the emplacement technique on sand-plaster mixtures. **A.** Homogeneous grain size  
 490 distribution in a poured 90-10 wt% sand-plaster sample vs. heterogeneous grain size distribution in a sieved 90-  
 491 10 wt% sand-plaster sample with alternating coarser (sand-dominated) and finer (plaster-dominated) grain size  
 492 layers; **B.** Densities of non-dried samples employed by pouring or sieving, or oven-dried samples poured and  
 493 compacted into the ring shear cell, and oven-dried poured and compacted samples in direct shear tests, tensile  
 494 tests and extension tests. The filled symbols indicate averages of the light-grey individual measurements. **C.**  
 495 Inferred porosities of poured, sieved and poured+compact samples.

497 **Table 2** – Density, porosity and humidity of sand and plaster and their mixtures in function of the method of emplacement described in Section 3 and Figure 4B-C; sieved and  
 498 poured samples were air-dried, poured+compacted samples were oven-dried;  $\rho$  = density;  $\varphi$  = porosity; uncertainties on sieved and poured densities are standard deviations  
 499 ( $1\sigma$ ), uncertainties on humidity indicate measurement precision relative to the total sample weight.

Sand:Plaster ratio (wt%)	Plaster (wt%)	$\rho_{\text{Sieved}}$ (kg.m <sup>-3</sup> )	$\rho_{\text{Poured}}$ (kg.m <sup>-3</sup> )	$\rho_{\text{Compacted}}$ (kg.m <sup>-3</sup> )	$\rho_{\text{Compacted ring shear}}$ (kg.m <sup>-3</sup> )	$\varphi_{\text{Sieved}}$ (vol%)	$\varphi_{\text{Poured}}$ (vol%)	$\varphi_{\text{Compacted}}$ (vol%)	$\varphi_{\text{Compacted ring shear}}$ (vol%)	Humidity Weight loss (wt%)
100:0 (Sand)	0	1410±5	1235±7	1700	1625±26	43.6	53.5	36.0	38.8	0.05±0.03
95:05	5	-	-	1680	1514±18	-	-	36.8	43.0	0.17±0.03
90:10	10	1327±6	1190±4	1666	1505±17	47.1	55.3	37.4	43.5	0.29±0.03
80:20	20	1237±8	1187±14	1650	1467±11	50.9	55.5	38.2	45.0	0.28±0.03
65:35	35	-	-	1465	1439±18	-	-	45.4	46.3	0.38±0.03
50:50	50	899±7	906±9	1268	1272±8	64.6	66.4	52.9	52.8	0.79±0.03
30:70	70	-	-	1125	1133±10	-	-	58.4	58.2	0.76±0.03
0:100 (Plaster)	100	-	-	900	901±2	78.1	76.7	67.0	67.0	1.03±0.03
0:100 (non-dried plaster)	100	564±6	636±11	900	-	-	-	67.0	-	-

## 501 4.2 Humidity tests

502 After 72 hours of oven-drying at 90°C, samples showed a cumulative weight loss that  
503 increased roughly linearly ( $R^2 = 0.93$ ) with increasing plaster content (Figure 5; Table 2).  
504 While plaster lost a cumulative 1.05 wt% of moisture, quartz sand only lost 0.05 wt%. For all  
505 samples, more than 90% of the weight loss occurred in the first 24 hours of oven-drying (see  
506 data in Poppe et al., 2021), suggesting that drying overnight should be sufficient to remove  
507 most of the humidity from granular materials prior to experimentation.  
508



509 **Figure 5** - Weight loss of sand-plaster mixtures of varying weight ratios after 72 hours of oven drying as a proxy  
510 for humidity contained within one sample per material.

511

## 512 4.3 Ring shear tests

### 513 4.3.1 *Effect of shear rate*

514 The shear stress in a 90:10 wt% air-dried sand-plaster mixture measured at a shear rate of 2.5  
515  $\text{mm}\cdot\text{min}^{-1}$  increased by 2% compared to that measured at 25  $\text{mm}\cdot\text{min}^{-1}$  (see data in Poppe et  
516 al., 2021). This observation indicates a weak dependency of the measured shear stress on  
517 shear rate. While we consider this effect quantitatively marginal compared to reported error  
518 margins, one may scale the friction coefficients reported here to the actual shear rate used or  
519 observed in experiments by a correction factor of 2% per order of magnitude deviation from  
520 the 6  $\text{mm}\cdot\text{min}^{-1}$  used in our ring shear tests.

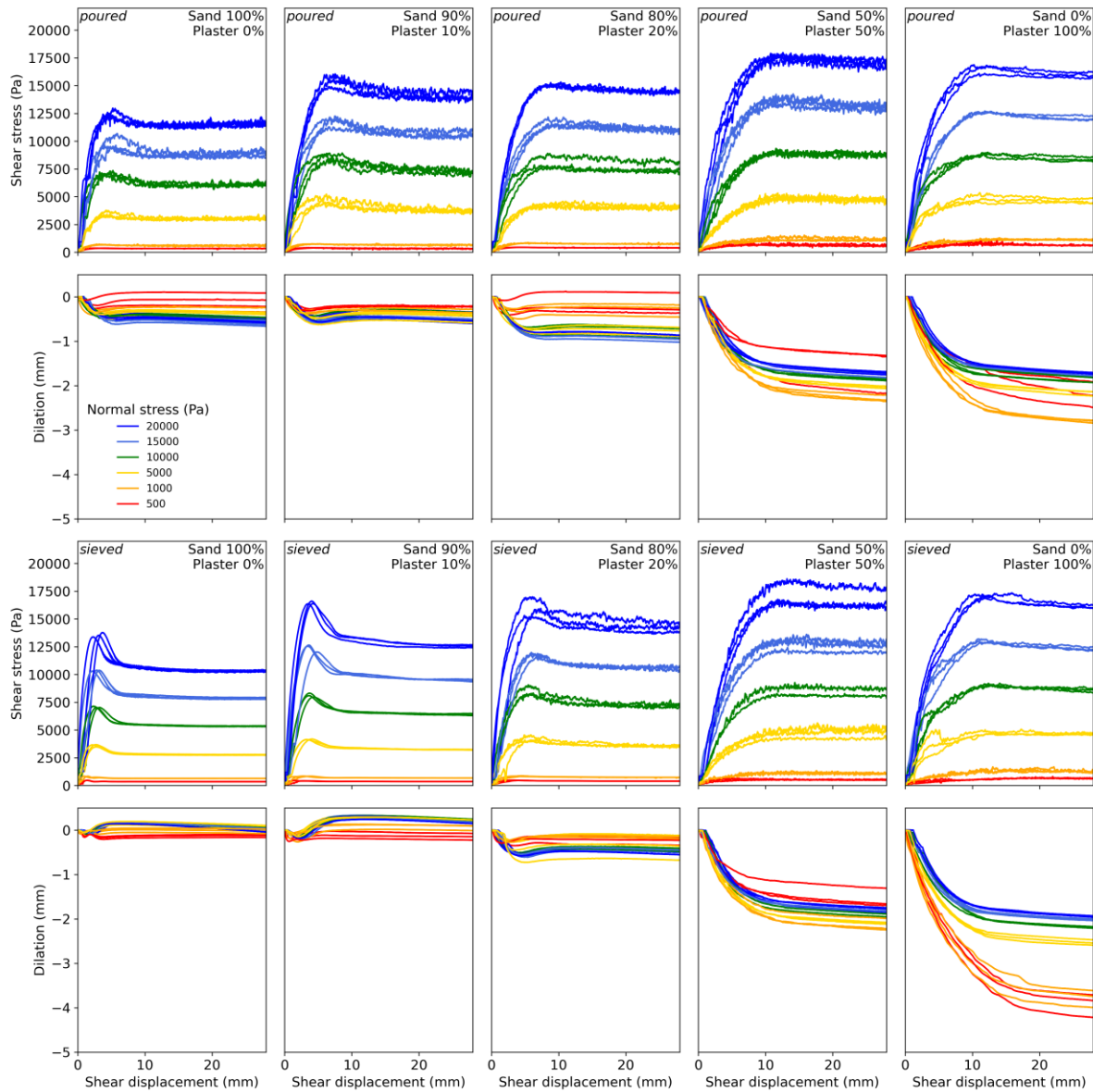
521

### 522 4.3.2 *Stress and dilation curves for air-dried uncompacted samples*

523 We performed 300 individual ring shear tests on poured or sieved, air-dried sand, plaster and  
524 sand-plaster mixtures with 10, 20 and 50 wt% plaster, and on oven-dried, poured+compacted  
525 sand, plaster and mixtures with 5, 10, 20, 35, 50 and 70 wt% plaster (see data in Poppe et al.,  
526 2021).

527 The shear stress and compaction curves for air-dried sieved or poured sand samples describe  
 528 the effect of the emplacement technique on the mechanical behaviour of sand-plaster mixtures  
 529 (Figure 6). Note that negative dilation by convention represents compaction (Lohrmann et al.,  
 530 2003).

531



532

533 **Figure 6 – A.** Shear stress ( $\tau$ ) and sample dilation evolution as a function of time for air-dry poured versus  
 534 sieved sand and plaster and 90:10, 80:20 and 50:50 mixing ratios. Ring shear test data (RST) at normal loads  
 535 ranging between 500 Pa and 20,000 Pa at constant shear rate. Sample dilation is measured as RST lid uplift  
 536 during shearing. Negative is compaction, positive is decompaction.

537

538 For sieved pure sand, shear stress and compaction evolution are qualitatively similar to what  
539 was observed previously for other silica sands (Klinkmüller et al., 2016; Lohrmann et al.,  
540 2003; Panien et al., 2006). After an initial phase of compaction during shear stress build-up,  
541 decompaction accompanies shear zone localisation and failure occurs at a peak shear strength  
542 value concurrent with the maximum decompaction rate. The measured shear stress then drops  
543 to a dynamic plateau value without further decompaction. Overall, the peak strengths and  
544 post-peak plateau strengths increase with increased normal loads.

545 As the plaster content increases in sieved samples, three alterations to this well-established  
546 shearing behaviour are seen (Figure 6, bottom rows). Firstly, the initial peak is wider; i.e.  
547 more strain is needed to localise a shear zone. Secondly, the associated stress drop gradually  
548 decreases, and a peak is absent from a 50:50 sand-plaster ratio onwards; i.e. the behaviour of  
549 plaster-dominated mixtures is more plastic. Additionally, the stable sliding strength at a given  
550 normal load generally increases with increased plaster content. Thirdly, the compaction-  
551 decompaction cycle observable in sand-dominated mixtures ( $\leq 20$  wt% plaster) is replaced by  
552 steady compaction during localisation in the plaster-dominated mixtures ( $\geq 50$  wt% plaster).

553 For poured samples, the temporal evolution of shear stress and decompaction is qualitatively  
554 similar to what has been observed for sieved samples (Figure 6, top rows). Nonetheless, there  
555 are some quantitative deviations. First, the peaks are generally wider (i.e. localisation requires  
556 more strain) and stress drops are smaller when poured compared to when sieved. Second,  
557 high-frequency noise indicates stick-slip, except for pure sand, and such noise is typically  
558 higher in amplitude compared to sieved samples. In sand-dominated samples, a clear initial  
559 peak with stress drop occurs again, although it is accompanied by a more subtle compaction-  
560 decompaction cycle (without net decompaction). In plaster-dominated poured mixtures, such  
561 a peak stress is again absent and is replaced by strain strengthening and sample compaction  
562 until the dynamic steady state is reached.

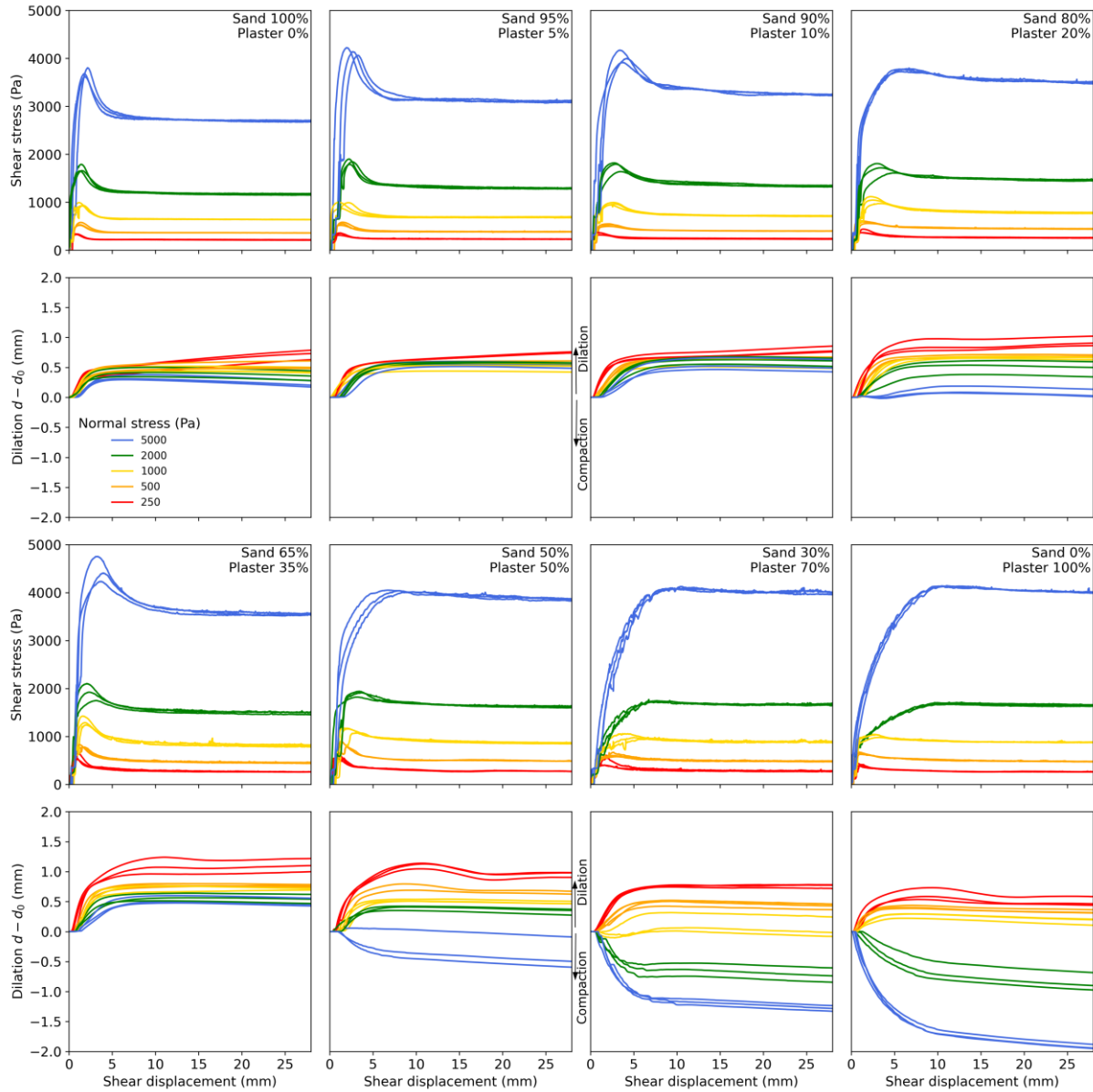
563

### 564 ***4.3.3 Stress and dilation curves for oven-dried compacted samples***

565 Figure 7 depicts the ring shear test results and dilation curves obtained for oven-dried sand,  
566 plaster and sand-plaster mixtures that were poured and mechanically compacted prior to  
567 testing. In general, the shear stress curves for these poured and pre-compacted samples are not  
568 as noisy as those for their poured and uncompacted equivalents (see Figure 6).

569 For sand-dominated mixtures ( $\leq 35$  wt% plaster), initial shear stress peaks are again present at  
570 all tested normal stresses. These materials thus display a similar strain hardening to strain

571 weakening behaviour, accompanied by compaction-decompaction cycles, as seen in the above  
 572 tests on air-dried samples and as described by (Panien et al., 2006).



573  
 574 **Figure 7:** Curves of shear stress versus shear displacement and of dilation for oven-dried, poured+compacted  
 575 sand, plaster and sand-plaster mixtures measured by using ring shear tests (n=120). Applied normal stresses  
 576 varied from 250 to 5000 Pa.

577 For plaster-dominated mixtures ( $\geq 50$  wt% plaster), a peak stress and compaction-  
 578 decompaction behaviour is also seen at low normal loads. This is more brittle behaviour than  
 579 the generally plastic behaviour seen in equivalent mixtures that were uncompacted prior to  
 580 testing (see Figure 5). In addition, stick-slip behaviour is apparent in the stress-displacement  
 581 curves at intermediate to high normal loads ( $>1000$  Pa). At high normal loads, the pre-  
 582 compacted plaster-dominated mixtures nonetheless again show pure strain hardening  
 583 behaviour without a stress drop and with compaction only (i.e. plastic behaviour). The

584 transition from somewhat brittle behaviour to entirely plastic behaviour occurs at decreasing  
585 normal stresses for increasing plaster contents. For a 50:50 wt% sand-plaster mixture, the  
586 transition lies between 2000-5000 Pa; for a 30:70 wt% mixture it lies between 1000-2000 Pa;  
587 for pure plaster it lies between 500-1000 Pa.

588

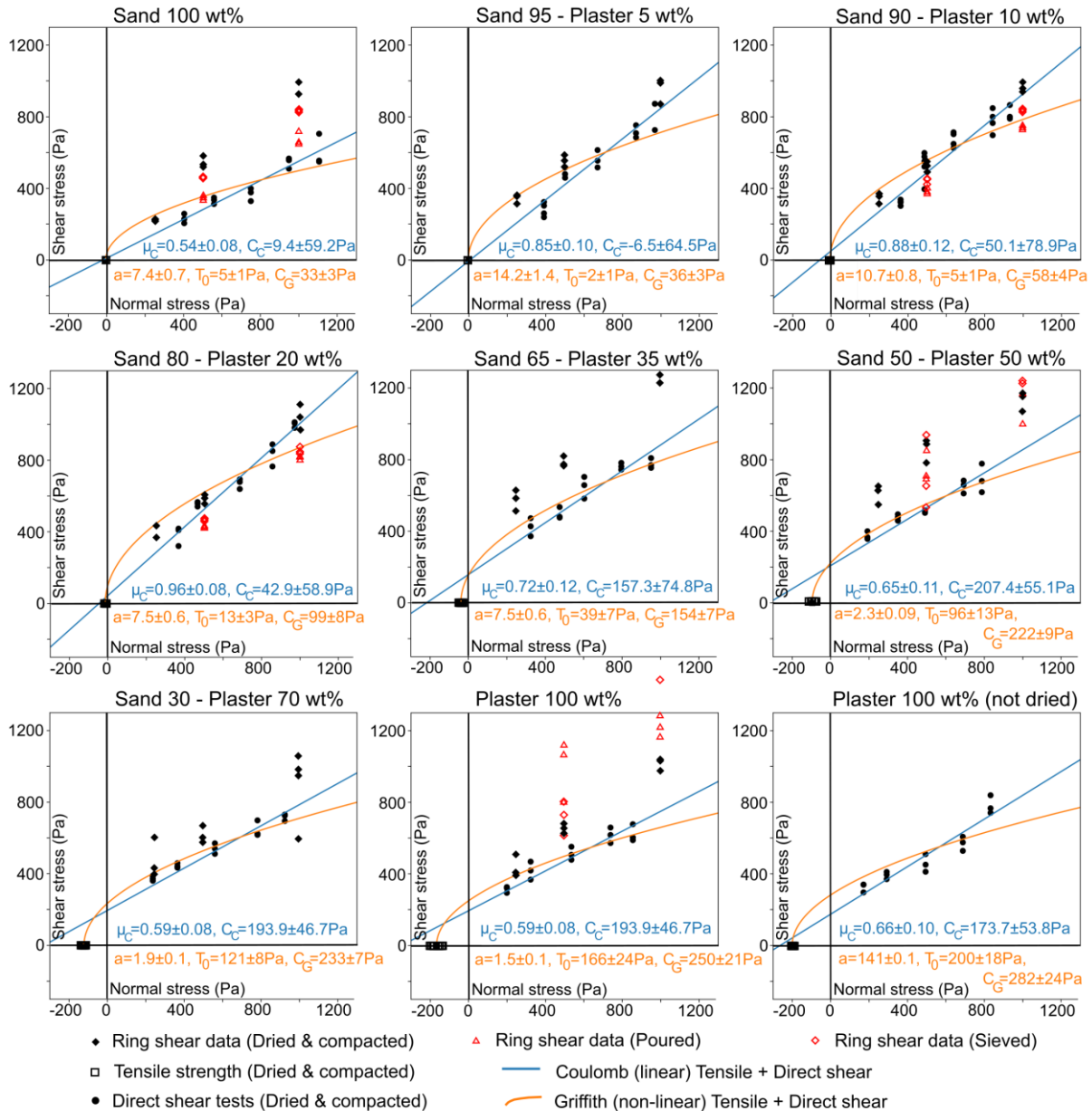
#### 589 ***4.3.4 Peak stress data from ring shear tests***

590 Peak stress generally increases with increased normal load for all materials regardless of  
591 emplacement procedure (Figure 8). The variation of peak strength with plaster content and  
592 emplacement technique is more complex, however.

593 For air-dried uncompacted samples, peak shear stresses for a given normal load generally  
594 increase with increased plaster content (Figure 8, red symbols). For sand-dominated sieved  
595 mixtures (Figure 8, red diamonds), peak shear stresses are higher than for sand-dominated  
596 poured mixtures (Figure 8, red triangles). For plaster-dominated sieved mixtures, on the other  
597 hand, peak shear stresses are lower than for plaster-dominated poured mixtures.

598 For oven-dried and compacted samples, a general increase in peak stress for a given normal  
599 load is not so clear (Figure 8, black diamonds). Rather, values generally increase up to 50  
600 wt% plaster, the peak stresses are similar for compacted and uncompacted samples. For pure  
601 plaster, however, the peak shear stress values of compacted samples are lower than those of  
602 non-compacted samples.





603 **Figure 8** – Shear stress ( $\tau$ ) versus normal stress ( $\sigma_n$ ) plots describing failure envelopes of oven-dried and  
 604 compacted sand and plaster and their mixtures, composed of tensile strengths ( $T_0$ ) obtained from tensile tests,  
 605 direct shear test results (with normal loads corrected for the silo effect, see Supplementary Materials) and ring  
 606 shear test results. Note that ring shear test data on sieved and poured samples were done on non-dried samples in  
 607 equilibrium with ambient air humidity. Optimal failure envelopes shown here are based on fitting a Coulomb  
 608 criterion (blue lines) or a Griffith criterion (orange curves) to direct shear and tensile test data on the oven-dried  
 609 and poured+compacted samples.

#### 610 611 **4.4 Direct shear tests**

612 We performed 143 direct shear tests on oven-dried poured+compacted sand, plaster and sand-  
 613 plaster mixtures and on air-dried poured+compacted plaster (Figure 8).

614

615 **4.4.1 Correction for the silo effect**

616 The results of the empirical correction for the ‘silo effect’ (Jansen, 1895; Mourgues and  
617 Cobbold, 2003) are shown in Supplementary Figure S1 and raw data in Poppe et al. (2021).  
618 The tested range of normal stresses overlaps with that of the three lowest normal load steps in  
619 the ring shear tests (250, 500 and 1000 Pa). The measured normal stress versus applied  
620 normal stress curves deviate from a 45° slope. This deviation is greatest for mixtures with 35  
621 and 50 wt% plaster. Therefore side-wall friction decreases the applied normal stress at the  
622 shear failure plane in all samples, and these curves enable a correction to obtain the average  
623 effective normal stress on the failure plane that was used to plot direct shear test data in  
624 Figure 8.

625  
626 **4.4.2 Shear strength of oven-dried and compacted samples**

627 The direct shear test results – i.e. shear strength values versus normal stress values that are  
628 corrected for the side-wall friction effect – are displayed in Figure 8 (black circles). For all  
629 mixtures, the shear strengths from the direct shear tests are lower than the peak strengths from  
630 the ring shear test results on oven-dried and poured+compacted samples, except for mixtures  
631 with 10 and 20 wt% plaster, where they are broadly similar for similar normal stresses.  
632 Overall, the direct shear test results describe approximately linear failure envelopes in shear –  
633 normal stress space. There is a general increase in shear strength at a given normal load as  
634 plaster content increases to about 20 wt%. With higher plaster contents, however, the shear  
635 strengths at the tested normal loads remain slightly higher than those of pure sand.

636  
637 **4.5 Tensile tests**

638 We performed 89 unconfined tensile tests on oven-dried and compacted sand, plaster and  
639 sand-plaster mixtures (Figure 9A; Table 3). Sand-plaster mixtures with < 20 wt% plaster  
640 display average tensile strengths that are near-zero (2-5 Pa) with little to no data spread. From  
641 20 wt% plaster upwards, the tensile strength increases with plaster content along a roughly  
642 linear trend ( $R^2 = 0.969$ ), up to a mean value  $167 \pm 23$  Pa for pure, oven-dried plaster. The  
643 data spread increases with increasing plaster content in a mixture. Non-dried plaster yields a  
644 tensile strength of  $200 \pm 18$  Pa, the mean of which is  $\sim 33$  Pa. This is almost 20% higher than,  
645 and statistically distinct from, the mean tensile strength value of oven-dried plaster ( $\alpha=0.050$ ;  
646  $p=0.004$ ;  $t$ -statistic=4.00,  $t$ -critical=2.31).

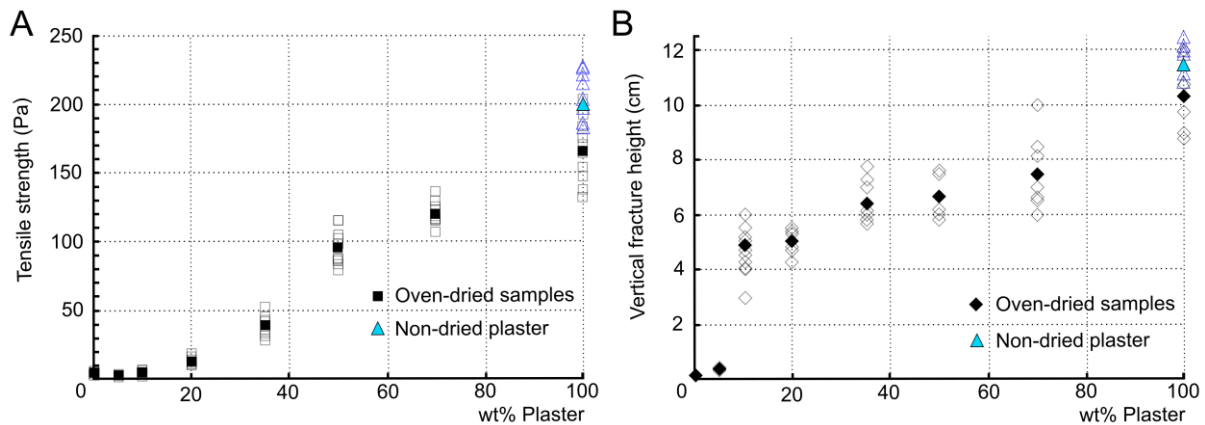
647  
648 **4.6 Extension tests**

649 We performed 25 extensional tests on oven-dried and compacted sand, plaster and sand-  
650 plaster mixtures, in which a total of 73 vertical opening-mode fracture portions were  
651 measured (Figure 9B; Table 3). Quartz sand extended in a diffuse manner and developed  
652 unmeasurably low cliffs. An arbitrary value of 0.1 cm, representing measurement limit, was  
653 therefore assigned here to pure sand.

654 From 10 wt% plaster upwards, open fractures were observed. With increasing plaster content,  
655 the height of the opening-mode fractures increases roughly linearly ( $R^2 = 0.899$ ). The material  
656 is able to develop opening-mode fractures to greater depths.

657 Non-dried plaster yielded vertical fracture heights that were on average 1.2 cm higher  
658 compared to oven-dried plaster. Despite their ranges overlapping, these averages are  
659 statistically distinct ( $\alpha=0.050$ ;  $p=0.046$ ;  $t\text{-statistic}=2.36$ ,  $t\text{-critical}=2.31$ ).

660



661

662 **Figure 9 – A.** Tensile strengths ( $T_0$ ) of sand and plaster and their mixtures as measured in tensile tests on oven-  
663 dried samples compacted by manual tapping. Unfilled symbols indicate individual measurements and therefore  
664 the uncertainty on the averages represented by the filled icons; **B.** Heights  $H$  of the vertical upper portions of  
665 normal (graben) faults formed in sand and plaster and their mixtures measured in extensional tests on oven-dried  
666 samples compacted by manual tapping. Unfilled icons show individual measurements and therefore indicate the  
667 uncertainty on the averages represented by the filled icons. Triangles in A. and B. represent individual  
668 measurements on air-dried plaster in equilibrium with laboratory ambient air humidity (20-30%).

669

670

671

672

673

674

675 **Table 3** – Physical properties of mixtures of oven-dried and compacted mixtures of quartz sand and plaster:  
676 tensile strength, vertical height of opening-mode fractures measured in extension tests, and Griffith cohesion  $C_G$   
677 derived from the former two parameters (bent lower part of failure envelope); \* marks non-dried plaster in  
678 equilibrium with ambient air humidity.

<b>Sand:Plaster ratio (wt%)</b>	<b>T<sub>0</sub> (Pa)</b>	<b>H (cm)</b>
100:0	5±1	0.1±0.5
95:5	2±1	0.4±0.8
90:10	5±1	4.9±0.4
80:20	13±3	5.0±0.4
65:35	39±7	6.4±0.7
50:50	96±13	6.6±0.7
30:70	121±8	7.5±1.3
0:100	166±24	10.3±1.1
0:100*	200±18	11.5±0.6

679

## 680 **5. Failure criterion analysis: Cohesion and friction coefficients**

### 681 **5.1 Theoretical background**

682 We determined the optimal fit to failure envelopes of sand-plaster mixtures by applying a  
683 linear Coulomb failure criterion and a non-linear Griffith failure criterion. The Coulomb  
684 failure criterion describes a linear relationship between the shear stress  $\tau$  on the failure plane  
685 and the effective normal stress  $\sigma_n$  acting on that plane:

$$686 (7) \tau = \mu_C \sigma_n + C_C,$$

687 where  $\mu_C$  is the Coulomb coefficient of internal friction or the slope of the line and  $C_C$  the  
688 Coulomb cohesion ('apparent' cohesion in Abdelmalak et al., 2016) derived from the  
689 intercept of the failure envelope with the  $y(\tau)$ -axis in a Mohr space diagram (Figure 1C). Such  
690 a linear relationship is commonly used to describe shear failure at relatively high normal  
691 stresses (i.e. high confining pressures, and thus greater depth) acting on rocks in the upper  
692 crust (Byerlee, 1978).

693 At low and negative (tensile) normal stresses (i.e. low confining pressure, and thus depth or  
694 with high fluid pressures), a non-linear failure envelope has been invoked to account for  
695 tensile and hybrid tensile/shear failure (Byerlee, 1978; Jaeger et al., 2007 and references  
696 therein). One commonly used non-linear envelope is the parabolic Griffith criterion (Jaeger et  
697 al., 2007; Labuz et al., 2018):

$$698 (8) \tau^2 = aT_0 (\sigma_n + T_0),$$

699 where  $a$  is a material-dependent constant and  $T_0$  is the tensile strength determined by the  
700  $x(\sigma_n)$ -axis intercept of the failure envelope in a shear - normal stress diagram (Figure 1C). The

701 intercept of the criterion with the  $y(\tau)$ -axis of the failure envelope defines the Griffith  
702 cohesion  $C_G$  of the material:

$$703 \quad (9) \quad C_G = T_0 \sqrt{\frac{a}{T_0} + 1}.$$

704 Cohesive powders often used in laboratory experiments yield values for constant  $a$  between 2  
705 and 4 (cfr. Abdelmalak et al., 2016).

706 We fitted Coulomb and Griffith failure criteria to failure envelopes that combined results of  
707 direct shear strength and tensile strength tests by using an adaptation of the ‘RST evaluation’  
708 Python script (Rudolf and Warsitzka, 2019). The Coulomb cohesion  $C_C$  and the Coulomb  
709 friction coefficient  $\mu_c$  were obtained by a 100-fold linear least-squares regression of the data  
710 plus noise to find the optimal fit of the linear Coulomb failure criterion in equation (7). The  
711 Griffith cohesion  $C_G$  was obtained by a 100-fold non-linear least-squares regression of the  
712 data plus noise to find the optimal fit of parameters  $a$  and  $T_0$  in equation (8).

713 We constrained optimal Coulomb and Griffith criteria for each of the oven-dried and  
714 compacted end-member materials and their mixtures, and for non-dried poured+compacted  
715 plaster (Figure 8). We then choose the best-fitting of these criteria to derive either a Coulomb  
716 cohesion ( $C_C$ ) or a Griffith cohesion ( $C_G$ ) value for each material. Since the slope of the  
717 Griffith criterion is non-unique, we used by default the optimal Coulomb criterion to derive a  
718 friction coefficient ( $\mu_C$ ) for each material.

719 We used only the peak strength data from the ring shear test results (poured, sieved, oven-  
720 dried and poured+compacted) to constrain an optimal Coulomb criterion as that is a standard  
721 approach in such tests (Klinkmüller et al., 2015; Montanari et al., 2017; Panien et al., 2006;  
722 Schulze, 1994). For comparison to the ring shear test results, we used only the shear strength  
723 data from the direct shear tests to constrain a Coulomb criterion for each material. This also  
724 enabled us to evaluate the added value of tensile test results in the failure criterion fitting.

725 We finally compared the obtained strength values to the Griffith cohesion  $C_G$  of the materials  
726 from combining average tensile strength from tensile tests with the vertical height of opening-  
727 mode fractures measured in extension tests. This approach follows the method proposed by  
728 Abdelmalak et al. (2016) and uses the approximation:

$$729 \quad (10) \quad C_G = T_0 \sqrt{\frac{H \rho g}{T_0} + 1}.$$

730

731 **5.2 Failure criterion fitting results**

732 A selection of the derived Coulomb ( $C_C$ ) and Griffith ( $C_G$ ) cohesions (Table 4) and friction  
 733 coefficients ( $\mu_C$ ) (Table 5) is displayed in Figure 10. For sand and sand-plaster mixtures with  
 734 plaster contents  $< 35$  wt%,  $C_C$  values from combinations of tensile strength data and direct  
 735 shear data (Figure 10A, green circles) yield the optimal fits (i.e. standard deviations are  
 736 smaller with respect to the cohesion values, see Table 4).  $C_G$  values obtained from tensile and  
 737 extension test data (Figure 10A, red squares), which are constrained only from data in the  
 738 tensile field, lie within the double standard deviations of  $C_C$  values, and increase from  $< 10$  Pa  
 739 to  $\sim 105$  Pa (Table 4).

740

741 **Table 4** – Cohesions of oven-dried and poured+compacted sand, plaster and sand-plaster  
 742 mixtures obtained from optimal fitting of linear Coulomb ( $C_C$ ,  $\mu_C$ ) and non-linear Griffith  
 743 ( $C_G$ ) failure criteria to various combinations of tensile strength, direct shear and ring shear test  
 744 results, and tensile strengths  $T_0$  and heights  $H$  of opening-mode fractures; \* marks air-dried  
 745 plaster.

Sand: Plaster ratio (wt%)	$C_C$ direct shear + $T_0$ (Pa)	$C_C$ direct shear (Pa)	$C_C$ ring shear compact (Pa)	$C_C$ ring shear poured (Pa)	$C_C$ ring shear sieved (Pa)	$C_G$ direct shear + $T_0$ (Pa)	$C_G$ ( $T_0 + H$ ) (Pa)
100:0	<b>4±21</b>	13±69	214±27	252±163	195±44	33±3	9.8±0.1
95:5	<b>12±24</b>	61±63	166±24	-	-	36±3	12.8±0.1
90:10	<b>16±29</b>	77±80	168±26	359±204	15±55	58±4	66.2±0.1
80:20	<b>18±28</b>	67±76	269±27	297±137	174±160	99±3	104.8±0.1
65:35	59±38	240±84	400±55	-	-	<b>154±7</b>	195.2±0.1
50:50	105±30	275±51	452±21	474±110	391±204	<b>222±9</b>	297.9±0.1
30:70	106±27	256±25	240±21	-	-	<b>233±7</b>	340.5±0.1
0:100	127±26	248±49	233±21	-	-	<b>250±21</b>	425.2±0.1
0:100*	157±22	192±68	-	672±105	615±85	<b>282±24</b>	494.9±0.1

746

747 For sand-plaster mixtures with plaster contents  $\geq 35$  wt%,  $C_C$  values systematically  
 748 overestimate the lower part of the failure envelope, whereas  $C_G$  provides optimal fit (Figure  
 749 10, orange circles). For direct shear test data alone in comparison,  $C_C$  provides larger standard  
 750 deviations and thus poorer fits (see Table 4).  $C_G$  values obtained from tensile strength and  
 751 direct shear data (Figure 10, orange circles) first continue increasing, albeit at a lower rate  $>$   
 752 50 wt% plaster, until the maximum of  $\sim 280$  Pa for pure plaster.  $C_G$  values obtained from  
 753 tensile and extension tests increase roughly linearly ( $R^2 = 0.965$ ) with increasing wt% plaster  
 754 content until a maximum of  $\sim 500$  Pa for non-dried compacted plaster (Table 4, Figure 10A).

755 Overall, the  $C_C$  values derived from ring shear data (Figure 10, green diamonds) are strongly  
 756 dependent on the higher normal stress data (5000 Pa) and their standard deviations are

757 systematically higher compared to those obtained from all other methods (Table 4). Their  $C_C$   
 758 values are highest of all obtained values for mixtures with plaster content  $\leq 50$  wt%, but  
 759 abruptly decrease to values similar to  $C_G$  values derives from failure envelopes that combine  
 760 tensile and direct shear test data.  $C_C$  values derived from direct shear data alone do not show  
 761 obvious trends, but they systematically have higher standard deviations compared to those  
 762 obtained from failure envelopes that combine tensile and direct shear test data and are  
 763 therefore not displayed on Figure 10A. Air-dried plaster yielded a  $C_G$  value that is  $\sim 50$  Pa  
 764 higher compared to oven-dried plaster, and displays relatively higher standard deviations  
 765 (Table 4, Figure 10A, blue-and-red circle).

766 Friction coefficient values can only be derived using a linear Coulomb criterion (Figure 10B,  
 767 Table 5).  $\mu_C$  values derived from tensile strengths and direct shear data (Figure 10B, green  
 768 circles) increase with increasing plaster content up to  $\leq 20$  wt%. For mixtures with a plaster  
 769 content  $\geq 35$  wt%,  $\mu_C$  values decrease again to about half of the value for plaster obtained  
 770 from ring shear data.

771  $\mu_C$  values obtained from ring shear data (Figure 10B, green diamonds) have much lower  
 772 standard deviations compared to those from combined tensile strengths and direct shear data  
 773 (Figure 10B, green circles), but produce no discernable trend. Values vary between 0.71 and  
 774 0.81, with an outlying minimum of 0.63 for non-dried plaster (Table 5).

775  $\mu_C$  values of non-dried plaster obtained either from direct shear data alone, or in combination  
 776 with tensile test data, agree very well (Table 5, Figure 10B, blue-and-red circle). These values  
 777 are slightly higher than those obtained for oven-dried plaster as constrained from tensile  
 778 strength and direct shear test data (Figure 10B, green circles), and they are lower than those  
 779 for oven-dried plaster as constrained from ring shear test data (Figure 10B, diamonds).

780

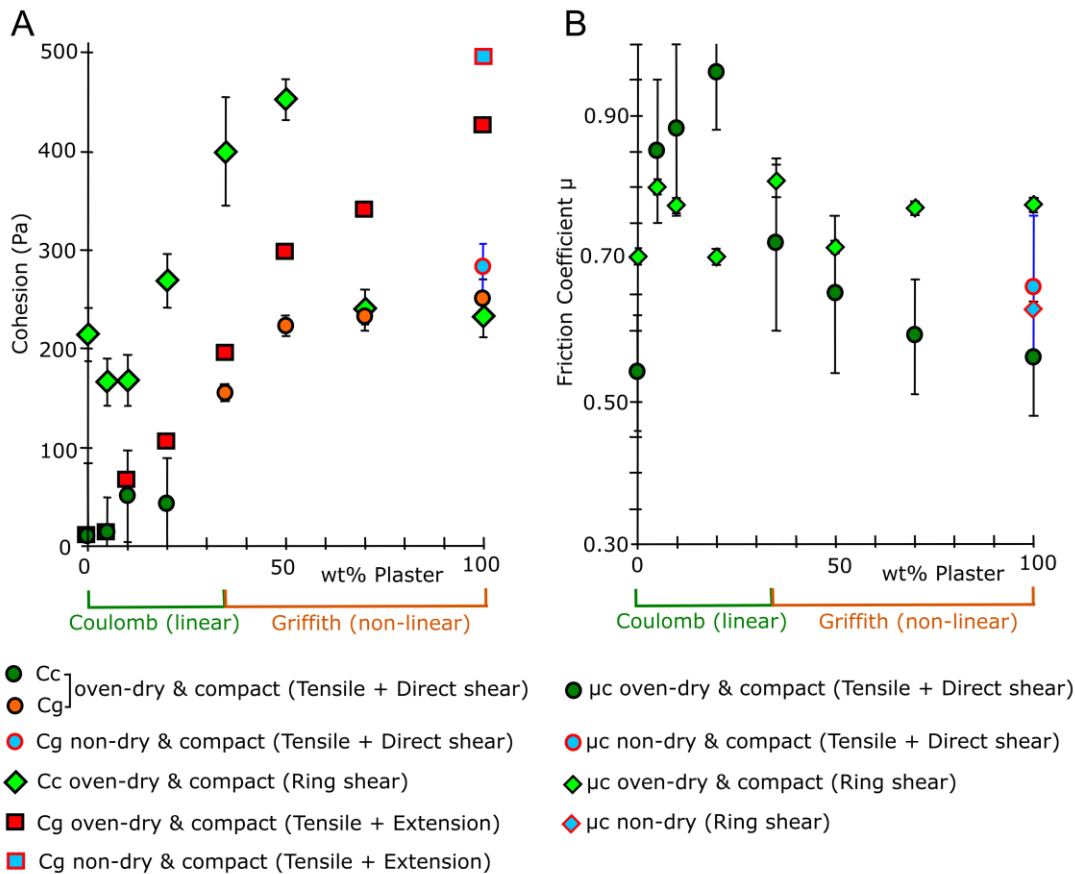
781

782

783 **Table 5** – Friction coefficients of oven-dried and compacted mixtures of quartz sand and plaster obtained from  
 784 optimal fitting of linear Coulomb ( $\mu_C$ ) failure criteria to failure envelopes of various combinations of tensile  
 785 strength, direct shear and ring shear test results; \* marks non-dried plaster in equilibrium with ambient air  
 786 humidity.

Sand:Plaster ratio (wt%)	$\mu_C$ direct shear + $T_0$	$\mu_C$ direct shear	$\mu_C$ RST compact	$\mu_C$ RST poured	$\mu_C$ RST sieved
100:0	0.54±0.08	0.48±0.08	0.70±0.01	0.64±0.02	0.67±0.01
95:5	0.85±0.10	0.61±0.08	0.80±0.01	-	-
90:10	0.88±0.12	0.85±0.13	0.77±0.01	0.78±0.02	0.82±0.01

80:20	0.96±0.08	0.85±0.09	0.70±0.01	0.80±0.01	0.76±0.01
65:35	0.72±0.12	0.55±0.11	0.81±0.02	-	-
50:50	0.65±0.11	0.48±0.08	0.72±0.01	0.88±0.01	0.85±0.02
30:70	0.59±0.08	0.41±0.03	0.77±0.01	-	-
0:100	0.56±0.08	0.43±0.08	0.76±0.01	-	-
0:100*	0.66±0.10	0.63±0.06	0.63±0.06	0.80±0.01	0.83±0.01



787 **Figure 10** – Regression results based on failure envelope reconstructions in shear-normal stress space using a  
 788 linear Coulomb failure criterion versus a non-linear Griffith one. **A.** Cohesion of compacted sand, plaster and  
 789 sand-plaster mixtures. Best-fit  $C_C$  (< 35 wt% plaster) or  $C_G$  (> 20 wt% plaster) values are displayed for the  
 790 combination of tensile and direct shear tests. Ring shear results are peak shear strengths. See Table 4. **B.** Friction  
 791 coefficient values  $\mu_C$  of compacted sand, plaster and sand-plaster mixtures for the combination of tensile and  
 792 direct shear test data or ring shear test data. See Table 5.

## 793 6. Discussion

### 794 6.1 Impact of material handling and humidity on material properties

795 It is well established that the mechanical properties of quartz sand differ significantly when  
 796 emplaced into a sand-box by sieving or pouring. Sieving produces higher sand pack density,  
 797 higher internal friction coefficient and a more brittle stress-strain behaviour – i.e. a sharper  
 798 stress peak and a larger post-peak stress drop, due to slower sedimentation rates during  
 799 sieving (Lohrmann et al., 2003; Panien et al., 2006). For pure quartz sand, our tests reproduce



800 such observations (Figures 4 and 6, Table 2). Density of pure sand can be further elevated by  
801 compaction – either through pressing (ring shear tests) or vibration (tapping). Our data  
802 indicate that compaction does not effect cohesion of pure sand (Table 4), but that it slightly  
803 increases the friction coefficient (Table 5).

804 For pure plaster, our tests document the opposite behaviour: sieved plaster is less dense,  
805 poured plaster more dense (Figure 4B, Table 2). We propose that friction with air during  
806 sieving might result in increased electro-static forces that increase porosity between settled  
807 plaster grains (van Gent et al., 2010). Pouring plaster may reduce electrostatic forces and may  
808 make plaster-rich packs more susceptible to compaction during emplacement. In terms of  
809 mechanical properties, our data show that sieved plaster compacts more at low normal loads  
810 compared to poured plaster (Figure 6). Sieving or pouring of pure, air-dried plaster produced  
811 a discernable difference in cohesion (Table 4), and sieving slightly increased the friction  
812 coefficient (Table 5). Even if assessed minimal, mineralogical changes due to oven-drying at  
813 90°C cannot be ruled out (Vimmrová et al., 2020). Drying in combination with mechanical  
814 compaction has a strong effect on the mechanical behaviour of pure plaster, however. In  
815 addition to higher bulk density and smoother stress-displacement curves, a more brittle  
816 behaviour is seen at low normal loads compared to poured or sieved oven-dried plaster  
817 (Figures 6 and 7), and cohesions and friction coefficients are lower regardless of shear testing  
818 approach and fitted failure criterion (Tables 4 and 5). SEM pictures showed that, in contrast to  
819 the (sub)rounded quartz sand grains, gypsum crystals are tabular gypsum to blocky.  
820 Compaction may thus reorient gypsum crystals toward alignment with the shear plane, thus  
821 making grain-grain sliding easier, and/or because reduced moisture content reduces the  
822 electrostatic attractions between plaster grains.

823 For a sand-plaster mixture with a plaster content of 50 wt%, there is no significant difference  
824 in the density when sieved or poured. In addition, sieving of sand-plaster mixtures results in  
825 layered, non-homogeneous grain size distribution throughout packs (Figure 4A). Thus,  
826 sieving devices that are designed to ensure an ideally dense packing of sand (e.g. Maillot  
827 2013) would create heterogeneous layering due to density, grain size and grain shape  
828 differences between quartz sand and gypsum particles. Similarly, Krantz (1991) showed that  
829 emplacement-induced density differences affect the shear strength of mixtures of quartz sand  
830 and cement more than the difference in particle density of sand versus cement. Pouring is also  
831 not ideal as it creates variations in grain packing density throughout sand-plaster mixtures.  
832 We surmise that these effects of pouring or sieving could be seen in our data to some extent.  
833 Poured samples, as well as sieved samples with high plaster content, generally show noisier

834 stress-displacement curves (Figure 6), although no clear trends or differences were seen in  
835 cohesion and friction values (Tables 4 and 5). Compaction and oven-drying had a strong  
836 effect on pure plaster. Smoother stress-displacement curves, a more brittle behaviour (stress  
837 drop) at low normal loads, and lower friction coefficients are consistently seen compared to  
838 non-dried and non-compacted equivalents (Table 4).

839 The problem of ambient humidity in granular analogues has received little attention, although  
840 in quartz sand, moisture is known to increase the bulk strength (van Mechelen, 2004). Sand-  
841 plaster mixtures in past studies have been used in equilibrium with ambient air humidity in  
842 laboratories, which can vary strongly from day to day influenced by the weather. Our data  
843 demonstrate that a sand-plaster mixture's humidity increases with increasing plaster content  
844 (Figure 5). The moisture uptake by gypsum powder from ambient humidity was previously  
845 measured to be ~2-2.5 wt% over 2.5 days under a constant air humidity of 75.2% (Lide,  
846 1995). Undried plaster used here contains on average 1 wt% of water (Figure 5). Our data  
847 further show that comparative test results of direct shear, tensile strength, and extension  
848 fracturing of pure air-dried plaster are statistically distinct from those of oven-dried plaster  
849 (Figures 8, 9 and 10). The strength of non-dried plaster is thus significantly affected by  
850 humidity. Importantly, the measurement uncertainties of the mechanical properties of non-  
851 dried plaster are higher as well. Our results establish that oven-drying sand-plaster mixtures to  
852 remove excess humidity prior to emplacement in a modelling apparatus should be pursued to  
853 increase reproducibility of the physical properties of the mixtures.

854 Except for Poppe et al. (2019), published experimental laboratory studies do not mention  
855 oven-drying sand-plaster mixtures prior to experimentation. Poppe et al. (2015) invoked  
856 variations in humidity of the sand-plaster mixtures from day to day to explain the occurrence  
857 of overburden stability in some experiments and overburden collapse in other experiments. In  
858 other experimental studies of geological deformation, the dip of fault planes formed in non-  
859 dried, poured sand-plaster piles has been systematically measured (Holohan et al., 2013;  
860 Rincón et al., 2018; Roche et al., 2001). That dip, however, depends on the angle of internal  
861 friction, which our results demonstrate in turn depends on material humidity and compaction.  
862 Furthermore, asymmetric development of model deformation in laboratory models of  
863 volcanic processes where cones have been traditionally poured has been attributed to set-up  
864 geometry asymmetry (e.g. Byrne et al., 2013; Delcamp et al., 2008; Kervyn et al., 2009;  
865 Merle and Borgia, 1996; Rincón et al., 2018; Van Wyk De Vries and Merle, 1998). Our  
866 results show that humidity and bulk density – i.e. porosity – variations may cause spatial and

867 temporal heterogeneities in the mechanical properties of sand-plaster mixtures that are  
868 unaccounted for.

869 Based on our results, we recommend oven-drying and compacting sand-plaster mixtures prior  
870 to their deformation in scaled laboratory models. We did not test chemical effects of heating  
871 on our gypsum material. While most significant effects have been shown to occur by heating  
872 above 100°C, heating up to 50°C for 24 hours may be tested to completely avoid effects on  
873 gypsum chemistry and strength (Park et al., 2010; Vimmrová et al., 2020).

874 Sand-plaster mixture ratios should be calculated by weight% (this study; Poppe et al., 2019)  
875 rather than by volume% (e.g. Delcamp et al., 2008; Poppe et al., 2015; Rincón et al., 2018;  
876 Roche et al., 2000; Zorn et al., 2020). Immediately after drying, mixtures should be cooled in  
877 a sealed container to prevent reabsorption of air moisture. During model set-up, a known mass  
878 of the mixture should be instantaneously poured into the sand-box and mechanically  
879 compacted down to a pre-determined bulk volume and thus a well constrained bulk density.  
880 That compaction can be achieved by manual tapping as in our direct shear, tensile and  
881 extension tests, by pre-loading and pressing the samples as in our ring shear tests, or by  
882 mechanical vibration (Galland et al., 2009; Poppe et al., 2019). This more consistent approach  
883 to material handling should help to better constrain bulk densities and porosities, to ensure  
884 homogeneous grain size and mineralogy distribution, to provide better control on mechanical  
885 properties, and promote greater confidence in the reproducibility of experimental outcomes  
886 involving sand-plaster mixtures.

887

## 888 **6.2 The silo effect in direct shear tests : empirical versus theoretical correction**

889 In a silo, side-wall friction counteracts gravity forces; this ‘silo effect’ or ‘Jansen effect’  
890 reduces the actual normal load acting on the shear plane in a direct shear test (Jansen, 1895).  
891 Most often, the linear Coulomb failure criterion is assumed to adequately fit failure envelopes  
892 of quartz sand that are reconstructed from direct shear tests, and quantify the sand’s cohesion  
893 and friction coefficient (e.g. Galland et al., 2006; Krantz, 1991; Lohrmann et al., 2003;  
894 Montanari et al., 2017; Schellart, 2000). When corrected theoretically for the silo effect, the  
895 failure envelopes gain a steeper slope and their intercept with the vertical axis decreases in  
896 absolute value (Mourgues and Cobbold, 2003). Mourgues and Cobbold (2003) set a  
897 theoretical threshold of sample height to cylinder diameter ratio of 0.5 to avoid the silo effect.  
898 That ratio is nevertheless as high as 1 in other studies (Abdelmalak et al., 2016; Schellart,  
899 2000). If unaccounted for, the silo effect results in underestimated internal friction  
900 coefficients and overestimated cohesions.

901 We have found empirically that side-wall friction progressively reduces the normal load at the  
902 failure plane in direct shear tests, even at low normal loads below that theoretical threshold  
903 value of 0.5 (see Supplementary Materials). Furthermore, we found that the silo effect  
904 increases with increasing plaster content, up to about 50 wt% plaster and then it decreases  
905 slightly, although it remain higher for pure plaster than for pure sand. Our empirical  
906 correction method yielded reduced effective normal loads, and thus produced failure  
907 envelopes with steeper slopes and with lower vertical axis intercepts in shear-normal stress  
908 space. As a result, the cohesion values of granular materials in past studies that ignore the silo  
909 effect are most likely overestimations (e.g. Abdelmalak et al., 2016; Lohrmann et al., 2003;  
910 Schellart, 2000). Similarly, friction coefficients estimated previously from direct shear tests  
911 without silo effect correction are likely underestimates. This empirical correction can be used  
912 when establishing new granular analogue materials, or retrospectively to correct published  
913 direct shear test results.

914

### 915 **6.3 Effects of plaster content on mechanical properties**

916 Our data show that for several measured physical or mechanical properties, such as bulk  
917 density, porosity, tensile strength, derived cohesions and friction coefficients, as well as the  
918 brittle or plastic behaviour of the material, are sensitive to the plaster content in a mixture  
919 regardless of handling procedure. In addition, trends in these properties differ for sand-rich  
920 mixtures (i.e.  $\leq 20$  wt% plaster content), compared to plaster-rich mixtures (i.e.  $\geq 35$  wt%  
921 plaster contents).

922 With increasing plaster content, there is an overall decrease in bulk density of a sand-plaster  
923 mixture and a corresponding increase in porosity (Figure 4B & C). Moreover, there is a  
924 notable increase in the rate of change of density or porosity with increased plaster content at  
925 20 wt% plaster content and higher. The bulk density of plaster is approximately half that of  
926 quartz sand, for the same handling and humidity (Figure 4B). Conversely, the inferred  
927 porosity of quartz sand is 35-55 vol% and that of plaster is 65-78 vol% (Figure 4C).  
928 Previously, van Gent et al. (2010) found a similar porosity of  $\sim 75$  vol% for gypsum powder.

929 SEM images and grain size distribution measurements showed that smaller gypsum crystals  
930 (mean diameter of 2-10  $\mu\text{m}$ ) can aggregate into clusters (Figure 2), which are too large to fill  
931 the pore space in between the larger sand grains (mean diameter of 180-250  $\mu\text{m}$ ). Therefore,  
932 although gypsum crystals have slightly greater density than quartz crystals (2730  $\text{kg}\cdot\text{m}^{-3}$  vs.  
933 2655  $\text{kg}\cdot\text{m}^{-3}$ ), the bulk density of a sand-plaster mixture possibly decreases as the plaster  
934 content increases because of the high micro-scale porosity of the gypsum aggregates (Figure

935 4B). The described grain size effects can be avoided by using mixtures of granular materials  
936 of similar grain sizes where only particle shape influences the material's strength, such as  
937 silica flour mixed with silica microbeads (Abdelmalak et al., 2016).

938 An increase in plaster content also generally leads to a more plastic behaviour of a sand-  
939 plaster mixture (Figures 6 & 7). The stress drop seen for sand-rich mixtures diminishes and  
940 ultimately disappears, especially at high normal stresses (<1000 Pa). An exception is when  
941 the mixture is oven-dried and pre-compacted; then a small stress drop persists in plaster-rich  
942 materials at low normal stresses (<1000 Pa). Irrespective of handling technique, the stress  
943 drop diminishes from about 20-35 wt% plaster content and upward. This general shift to a  
944 more plastic behaviour in stress-displacement curves as plaster content increases corresponds  
945 to a change in dilation behaviour. Sand-rich mixtures (<35 wt% plaster) compact prior to  
946 sample failure then de-compact, as previously observed for pure sand (Panien et al., 2006;  
947 Ritter et al., 2016). Plaster-rich samples (>35 wt% plaster) undergo compaction throughout  
948 shearing. Numerical simulations of deformation of granular materials produce a similar  
949 transition to more plastic and compaction-dominated behaviour with increased porosity (cfr.  
950 Figure 4 in Schöpfer et al., 2009). Therefore, we tentatively attribute the change to a more  
951 plastic behaviour with increased plaster content to increased bulk porosity. This change may  
952 occur with more distributed strain localisation in the more porous plaster-rich mixtures,  
953 especially at high normal stresses, as the progressive collapse of pore-spaces in the gypsum  
954 crystal aggregates inhibits the formation of well-defined shear zones.

955 Sand-plaster mixtures therefore have the capacity, like real rocks, to display a brittle-plastic  
956 transition with depth. Considering the normal stress as equivalent to confining pressure of an  
957 overburden and assuming the compacted bulk densities in Table 2, that transitional depth  
958 would amount to 30 cm height (i.e. at ~5000 Pa) in mixtures with 20 wt% plaster. This depth  
959 would be shallower with increased plaster content, and it would lie at ~16 cm (~2000 Pa) with  
960 50 wt% plaster and at 11 cm (~1000 Pa) in pure plaster. This brittle to plastic transition  
961 primarily represents a change in strain-weakening or strain-strengthening behaviour, and does  
962 not necessarily imply a major change in strain localisation (i.e. shear zone vs. distributed  
963 flow) with depth within a material.

964 Associations between increased plaster content and a sand-plaster mixture's strength, in terms  
965 of cohesion and friction coefficient, are complex and in part dependent on measurement  
966 technique. In general, cohesion increases with increasing plaster content, up to about 50 wt %  
967 plaster (Figure 10A, Table 4). Coulomb cohesions thereafter decrease or stabilize, whereas  
968 Griffith cohesions continue to increase with increased plaster content. The friction coefficient

969 either shows no clear trend with increasing plaster content (ring shear test data) or shows an  
970 initial slight increase at 0-20 wt% plaster followed by overall decrease at 20-100 wt% plaster  
971 (Figure 10B, Table 5). Uniaxial compressive strength of quartz crystals at room temperature  
972 and pressure is around 190-300 MPa (and references therein Scholz, 1972), whereas ultimate  
973 shear strength of gypsum crystals is around 0.6 – 18 MPa (Williams, 1988). Furthermore,  
974 gypsum possesses anisotropic strength, further complicating the mechanical behavior of  
975 stressed plaster packs (Sarkar and Mitra, 2019; Vimmrová et al., 2020 and references therein).  
976 Such crystal strengths far exceed the differential stresses applied in our material tests. The  
977 friction coefficient of granular materials in a regime of no grain fracture is known to increase  
978 with increased grain surface roughness (angularity) and particle size distribution (Mair et al.,  
979 2002), and it is known to decrease with increased porosity (Schöpfer et al., 2009). Moreover,  
980 stick-slip behaviour in deformed granular materials is associated with smoother grain surfaces  
981 (Mair et al., 2002; Rosenau et al., 2009). Therefore, we interpret that cohesions and friction  
982 coefficients at plaster contents of up to 20-50 wt % initially increase because of increased  
983 particle size distribution on mixing relatively coarse quartz sand with relatively fine gypsum  
984 powder (Figure 2). Increased inter-crystal attraction forces in gypsum may also play a role in  
985 that initial strength increase (see below). Cohesion and friction coefficient subsequently  
986 decrease or stabilize at plaster contents of up to 50-100 wt % because of increased porosity  
987 (Figure 4) and possibly also the capability of gypsum grains to align and to slip past each  
988 other along their relatively smooth crystal faces. The latter factor can also account for the  
989 short-frequency noise and stick-slip events observed in plaster-rich mixtures (Figure 6 & 7).  
990 Increasing plaster content of sand-plaster mixtures is clearly associated with increased tensile  
991 strength. This has been known qualitatively from the occurrence of opening mode fractures in  
992 such mixtures compared to the absence of such fractures in pure quartz sand, and has formed  
993 a main reason for use of plaster veneers or sand-plaster mixtures previously (e.g. Byrne et al.,  
994 2013; Holohan et al., 2008; Poppe et al., 2015; Roche et al., 2001; Shea and van Wyk de  
995 Vries, 2008; van Gent et al., 2010). Here, we quantify the tensile strength increase, and we  
996 show again that its rate increases sharply at  $\geq 20$  wt% plaster content (Figure 9A). The high  
997 tensile strength of plaster relative to quartz sand, and the corresponding increase in tensile  
998 strength with increased plaster content in mixtures, are potentially related to the increased  
999 effectiveness of electrostatic attraction forces that bond gypsum crystals. Tensile strength has  
1000 been shown to decrease slightly with porosity in numerical simulations of the deformation of  
1001 granular material, but to increase greatly with increased proportion of bonded contacts  
1002 between particles (Schöpfer et al., 2009). Atomic Force Microscopy experiments show that

1003 gypsum crystal faces are attracted to each other by van der Waal's forces and electrostatic  
1004 forces, which are supplemented by capillary forces at high relative humidity (Finot et al.,  
1005 2001). In general, therefore, an increase in such attraction forces with increased plaster  
1006 content in sand-plaster mixtures can account for the increased tensile strength of such  
1007 mixtures. The increase in inter-crystal force attraction with increased humidity also explains  
1008 the still greater tensile strength of pure undried plaster. Overall, these data confirm that using  
1009 plaster as a filler in sand is a valid strategy to increase and control such a mixture's tensile  
1010 strength.

1011

#### 1012 **6.4 Empirically reconstructed failure envelopes and theoretical failure criteria**

1013 Ring shear tests and direct shear tests on oven-dried and pre-compacted samples give slightly  
1014 different failure envelopes in the compressive stress field and consequently give different  
1015 values of cohesion and friction coefficient (Tables 4 & 5, Figure 10). While ring shear tests  
1016 reportedly yield accurate estimates of friction coefficients of sands with low standard  
1017 deviations, the method has yielded unrealistically high cohesions with large standard errors  
1018 from linear Coulomb extrapolations (Klinkmüller et al., 2015; Montanari et al., 2017; Panien  
1019 et al., 2006; Ritter et al., 2016). Furthermore, ring shear tests are difficult to operate at small  
1020 normal loads (<500 Pa), whereas direct shear tests are better suited to constrain this lower  
1021 part. Ritter et al. (2016) inferred that in ring shear tests the through-going shear zone likely  
1022 develops via the linkage of several shear zones, each initiated at one of the intruding lid  
1023 blades. In contrast, a through-going shear zone likely develops more readily as a single shear  
1024 failure plane in direct shear tests. This contrast in test methodology may at least partially  
1025 explain the mismatch between failure envelopes derived from ring shear test results and direct  
1026 shear test results (Figure 8), and consequently the values of cohesions and friction coefficients  
1027 derived from the linear Coulomb criterion (Figure 10).

1028 Cohesion values obtained for oven-dried and pre-compacted sand-plaster mixtures by  
1029 extrapolation of shear strength only ( $C_C$ ) shows different trends to those obtained by  
1030 extrapolation of tensile strength and extensional test data only ( $C_G$ ) (Table 4). Cohesions from  
1031 direct shear test or ring shear tests, despite differences in absolute values, show a similar  
1032 initial increase at low plaster contents followed by a decrease or levelling off at high plaster  
1033 contents (Figure 10). In comparison, cohesions obtained from combining tensile strength data  
1034 with extension tests yield a more monotonic linear increase of cohesion from near-zero for  
1035 sand to >400 Pa for plaster. The latter method is based on a non-linear Griffith criterion that  
1036 ignores data in the compressive field (Abdelmalak et al., 2016), however, and the resulting

1037 monotonic increase in cohesion that it yields is highly dependent on the measured value of  
1038 tensile strength (Equation 10), which itself increases linearly with plaster content (Figure 9).  
1039 In general, we therefore regard the cohesion and friction values constrained by interpolation  
1040 between data in both tensile and compressive fields to be more reliable than those constrained  
1041 by extrapolation from data in one field only. We find that linear Coulomb failure criteria more  
1042 optimally fit the combined tensile strength and direct shear data of sand-rich mixtures (<35  
1043 wt% plaster), whereas non-linear Griffith failure criteria better fit the combined tensile and  
1044 shear data of sand-plaster mixtures with  $\geq 35$  wt% plaster content. The addition of tensile  
1045 strength data in criterion fitting considerably helps to constrain the lower – negative – part of  
1046 the failure criteria (Table 4, Table 5). The resulting ‘preferred’ cohesion values (Figure 10A)  
1047 increase from near-zero for pure quartz sand to 200-250 Pa for sand-plaster mixtures with  $\geq$   
1048 50 wt% plaster. Similarly the ‘preferred’ friction coefficient values derived from Coulomb  
1049 criteria fitted to data in both tensile and compressive fields (Figure 10B) increase from  $\sim 0.54$   
1050 for pure quartz sand to  $\sim 0.96$  for mixtures with 20 wt% plaster and then decrease to  $\sim 0.56$  for  
1051 pure plaster. The more optimal fit of a non-linear Griffith failure criterion to sand-plaster  
1052 mixtures with a plaster content  $\geq 35$  wt%, shows that, in detail, the internal friction coefficient  
1053 of such mixtures is not constant throughout a sandbox model, but rather varies with depth – as  
1054 is the case for rock masses in nature. The fit of other non-linear failure criteria, such as that of  
1055 Hoek-Brown (Jaeger et al., 2007; Labuz et al., 2018) for such mixtures could be explored in  
1056 the future.

1057

## 1058 **6.5 Implications for scaling analogue models of crustal deformation**

1059 The combination of mechanical laboratory tests has shown that by systematically controlling  
1060 the weight ratio of quartz sand to plaster, analogue granular materials of varying strengths but  
1061 also brittle to complex brittle-plastic shear stress behaviour can be obtained. Compared to  
1062 pure sand, these properties allow analogue modelers to simulate a greater range of tensile to  
1063 shear fracturing, brittle to plastic behaviour, similar to how natural rocks are known to behave  
1064 in the shallow crust (e.g. Byerlee, 1978, 1968; Jaeger et al., 2007). Our characterisation now  
1065 quantifies values of cohesions and friction coefficients for sand-plaster mixtures (Tables 4 and  
1066 5) and shows that they are suitable to simulate natural rock strengths in scaled laboratory  
1067 models (Table 1). The comparison of failure criteria fits, however, also exposes the  
1068 uncertainties related to applying theoretical models to describe the complex, non-linear  
1069 rheology of granular analogue materials. Tensile strengths, in addition, might provide a  
1070 complementary or more direct means to scale laboratory experiments where opening-mode



1071 failure is important. This is the case for example in simulations of magma-filled fracture  
1072 opening that forms sheet intrusions (Galland et al., 2018; Poppe et al., 2019; Rivalta et al.,  
1073 2015), or in some tectonic extension experiments (e.g. Reber et al., 2020; Schreurs et al.,  
1074 2006). The newly quantified values of tensile strength, cohesion and friction coefficient of  
1075 sand-plaster mixtures now allow to systematically explore the effect of analogue granular  
1076 material strength as an experimental parameter.

1077

## 1078 **7. Summary and conclusions**

1079 Our study confirms that mixtures of quartz sand and gypsum powder – i.e. plaster – possess a  
1080 range of strengths and brittle to brittle-plastic behaviour that is analogue to that of crustal  
1081 rocks. By using a combination of density measurements, shear tests, tensile tests and  
1082 extension tests, we have constrained the effect of the emplacement technique and humidity,  
1083 and have constrained the shear and tensile strengths of density-controlled, oven-dried samples  
1084 of sand, plaster and sand-plaster mixtures.

1085 We found that:

- 1086 - Sieved sand is denser and less porous compared to poured sand; sieved plaster is  
1087 conversely less dense and more porous compared to poured plaster; the effects for  
1088 sand-plaster mixtures lie in between the two end-members.
- 1089 - While sieving or pouring sand-plaster mixtures introduces compositional and bulk  
1090 density heterogeneity (layering), pouring followed by mechanical compaction  
1091 produces more controlled and laterally consistent density while minimizing  
1092 mineralogical heterogeneity.
- 1093 - Humidity increases the strength of plaster and increases the uncertainty in the  
1094 measured mechanical properties.

1095 The plaster content and the applied normal stress constrain a brittle-plastic transition. The  
1096 stress-displacement behaviour of sand-rich sand-plaster mixtures ( $\leq 20$  wt% plaster) is  
1097 dominantly brittle, while plaster-rich sand-plaster mixtures ( $\geq 35$  wt% plaster) exhibit  
1098 more complex, plastic behaviour. We infer that this transition is ultimately controlled by a  
1099 porosity increase with increasing plaster content. We found that absolute tensile strength  
1100 of a sand-plaster mixture increases near-linearly with increased plaster content from near-  
1101 zero for pure quartz sand to  $166 \pm 24$  Pa for pure plaster. This value also increased with  
1102 increased humidity.

1103 For oven-dried, poured and compacted sand-plaster mixtures, a linear Coulomb failure  
1104 criterion fits most optimally to failure envelopes for  $\leq 20$  wt% plaster as constrained by

1105 both tensile strength and direct shear test data. A non-linear Griffith failure criterion most  
1106 optimally fits the failure envelopes for sand-plaster mixtures with  $\geq 35$  wt% plaster. Our  
1107 comparison of empirical mechanical testing methods suggests that the best-fit cohesions  
1108 most likely range from  $\sim 0$  Pa for quartz sand to  $\sim 250$  Pa for pure plaster, while Coulomb  
1109 friction coefficients range from 0.50 to 0.94, respectively. The more optimal fit to a non-  
1110 linear failure criterion suggests that in detail friction coefficients likely vary with depth  
1111 within a sand-plaster mixture with  $\geq 35$  wt% plaster. The non-linear relationship of  
1112 cohesion and friction coefficient to plaster content likely reflects a complex interplay of  
1113 factors controlling material strength, such as porosity, attraction forces between gypsum  
1114 crystals and contrasts between quartz and gypsum crystals in grain shape anisotropy, size  
1115 and smoothness.

1116 To obtain reproducible composition and mechanical properties, we recommend that sand-  
1117 plaster mixtures should be oven-dried for at least 24 hours to remove ambient humidity  
1118 and be poured and compacted mechanically to a controlled bulk density. Using these best-  
1119 practice recommendations, the characterised mechanical properties will provide a more  
1120 robust basis for using sand-plaster mixtures in laboratory-scale simulation of natural rock-  
1121 mass deformation.

1122

### 1123 **Author credit statement**

1124 S. Poppe: Conceptualization, methodology, data curation, investigation, formal analysis,  
1125 visualization, writing. E. P. Holohan: Conceptualization, methodology, supervision, writing –  
1126 review & editing. M. Rudolf: Methodology, formal analysis, investigation, visualization,  
1127 writing – review & editing. M. Rosenau: Methodology, supervision, writing – review &  
1128 editing. O. Galland: Methodology, writing – review & editing. A. Delcamp:  
1129 Conceptualization, methodology, writing – review & editing. M. Kervyn: Conceptualization,  
1130 methodology, supervision, writing – review & editing.

### 1131 **Declaration of interest statement**

1132 The authors declare that no conflict of interest exists with this work.

### 1133 **Data availability**

1134 The original data collected for this study is part of a GFZ open-access data publication (Poppe  
1135 et al., 2021). This data set also contains mechanical test data for garnet sand and kaolin clay  
1136 powder mixed with quartz sand as used in Grosse et al. (2020) and is available at  
1137 [https://dataservices.gfz-potsdam.de/panmetaworks/showshort.php?id=70f16b23-751b-11eb-  
1138 9603-497c92695674](https://dataservices.gfz-potsdam.de/panmetaworks/showshort.php?id=70f16b23-751b-11eb-9603-497c92695674)

1139

1140 **Acknowledgments**

1141 SP was supported during 2014-2019 by an Aspirant PhD fellowship from the Flemish Fund  
1142 for Scientific Research FWO-Flanders, Belgium, and a Vocatio grant, and since October 2020  
1143 by a frs-FNRS postdoctoral fellowship at ULB, Brussels. Régis Mourgues granted access to  
1144 the tensile test apparatus of the Geology Department of the University of Maine, France, and  
1145 kindly donated the Hubert-type shear test apparatus installed now at VUB. We thank Luc  
1146 Deriemaeker at VUB and Christelle Gruber at Univ. Maine for technical lab support and set-  
1147 up construction. We thank K. Elger and the GFZ Data Services for making our data set  
1148 publicly available. This work benefited from fruitful discussions with J. Kavanagh, S.  
1149 Burchardt, M. Abdelmalak, B. van Wyk de Vries, P. Grosse and many others.

1150

1151 **References**

- 1152 Abdelmalak, M.M., Bulois, C., Mourgues, R., Galland, O., Legland, J.B., Gruber, C., 2016.  
1153 Description of new dry granular materials of variable cohesion and friction coefficient:  
1154 Implications for laboratory modeling of the brittle crust. *Tectonophysics* 684, 39–51.  
1155 <https://doi.org/10.1016/j.tecto.2016.03.003>
- 1156 Adam, J., Klinkmüller, M., Schreurs, G., Wieneke, B., 2013. Quantitative 3D strain analysis  
1157 in analogue experiments simulating tectonic deformation: Integration of X-ray computed  
1158 tomography and digital volume correlation techniques. *J. Struct. Geol.* 55, 127–149.  
1159 <https://doi.org/10.1016/j.jsg.2013.07.011>
- 1160 Adam, J., Urai, J.L., Wieneke, B., Oncken, O., Pfeiffer, K., Kukowski, N., Lohrmann, J.,  
1161 Hoth, S., van der Zee, W., Schmatz, J., 2005. Shear localisation and strain distribution  
1162 during tectonic faulting - New insights from granular-flow experiments and high-  
1163 resolution optical image correlation techniques. *J. Struct. Geol.* 27, 299–301.  
1164 <https://doi.org/10.1016/j.jsg.2004.08.008>
- 1165 Barenblatt, G.I., 2003. *Scaling*. Cambridge University Press.
- 1166 Bertelsen, H.S., Rogers, B.D., Galland, O., Dumazer, G., Benanni, A., 2018. Laboratory  
1167 modeling of coeval brittle and ductile deformation during magma emplacement into  
1168 viscoelastic rocks. *Front. Earth Sci.* 6. <https://doi.org/10.3389/feart.2018.00199>
- 1169 Byerlee, J., 1978. Friction of rocks. *Pure Appl. Geophys.* 116, 615–626.  
1170 <https://doi.org/10.1007/BF00876528>
- 1171 Byerlee, J.D., 1968. Brittle-ductile transition in rocks. *J. Geophys. Res.* 73, 4741–4750.  
1172 <https://doi.org/10.1029/JB073i014p04741>
- 1173 Byrne, P.K., Holohan, E.P., Kervyn, M., Van Wyk de Vries, B., Troll, V.R., 2015. Analogue  
1174 modelling of volcano flank terrace formation on Mars. *Geol. Soc. Spec. Publ.* 401, 185–

1175 202. <https://doi.org/10.1144/SP401.14>

1176 Byrne, P.K., Holohan, E.P., Kervyn, M., Van Wyk de Vries, B., Troll, V.R., Murray, J.B.,  
1177 2013. A sagging-spreading continuum of large volcano structure. *Geology* 41, 339–342.  
1178 <https://doi.org/10.1130/G33990.1>

1179 Coulomb, C., 1773. Test on the applications of the rules of maxima and minima to some  
1180 problems of statics related to architecture. *Mem. Math. phys* 7, 343-382.

1181 Cruz, L., Malinski, J., Wilson, A., Take, W.A., Hilley, G., 2010. Erosional control of the  
1182 kinematics and geometry of fold-and-thrust belts imaged in a physical and numerical  
1183 sandbox. *J. Geophys. Res. Solid Earth* 115, 1–15. <https://doi.org/10.1029/2010JB007472>

1184 Cubas, N., Barnes, C., Maillot, B., 2013. Inverse method applied to a sand wedge: Estimation  
1185 of friction parameters and uncertainty analysis. *J. Struct. Geol.* 55, 101–113.  
1186 <https://doi.org/10.1016/j.jsg.2013.07.003>

1187 Davy, P., Cobbold, P.R., 1991. Experiments on shortening of a 4-layer model of the  
1188 continental lithosphere. *Tectonophysics* 188, 1–25. [https://doi.org/10.1016/0040-](https://doi.org/10.1016/0040-1951(91)90311-F)  
1189 [1951\(91\)90311-F](https://doi.org/10.1016/0040-1951(91)90311-F)

1190 Delcamp, A., van Wyk de Vries, B., James, M.R., 2008. The influence of edifice slope and  
1191 substrata on volcano spreading. *J. Volcanol. Geotherm. Res.* 177, 925–943.  
1192 <https://doi.org/10.1016/j.jvolgeores.2008.07.014>

1193 Donnadieu, F., Merle, O., Besson, J.C., 2001. Volcanic edifice stability during cryptodome  
1194 intrusion. *Bull. Volcanol.* 63, 61–72. <https://doi.org/10.1007/s004450000122>

1195 Dooley, T.P., Schreurs, G., 2012. Analogue modelling of intraplate strike-slip tectonics: A  
1196 review and new experimental results. *Tectonophysics* 574–575, 1–71.  
1197 <https://doi.org/10.1016/j.tecto.2012.05.030>

1198 Eisenstadt, G., Sims, D., 2005. Evaluating sand and clay models: Do rheological differences  
1199 matter? *J. Struct. Geol.* 27, 1399–1412. <https://doi.org/10.1016/j.jsg.2005.04.010>

1200 Finot, E., Lesniewska, E., Goudonnet, J.P., Mutin, J.C., Domenech, M., At Kadi, A., 2001.  
1201 Correlating surface forces with surface reactivity of gypsum crystals by atomic force  
1202 microscopy. Comparison with rheological properties of plaster. *Solid State Ionics* 141–  
1203 142, 39–46. [https://doi.org/10.1016/S0167-2738\(01\)00718-4](https://doi.org/10.1016/S0167-2738(01)00718-4)

1204 Galland, O., Bertelsen, H.S., Guldstrand, F., Girod, L., Johannessen, R.F., Bjugger, F.,  
1205 Burchardt, S., Mair, K., 2016. Application of open-source photogrammetric software  
1206 MicMac for monitoring surface deformation in laboratory models. *J. Geophys. Res.*  
1207 *Earth* 1–21. <https://doi.org/10.1002/2015JB012755>.

1208 Galland, O., Burchardt, S., Hallot, E., Mourgues, R., Bulois, C., 2014. Dynamics of dikes

1209 versus cone sheets in volcanic systems. *J. Geophys. Res. Solid Earth* 119, 6178–6192.  
1210 <https://doi.org/10.1002/2014JB011059>. Received

1211 Galland, O., Cobbold, P.R., Hallot, E., de Bremond d’Ars, J., Delavaud, G., 2006. Use of  
1212 vegetable oil and silica powder for scale modelling of magmatic intrusion in a deforming  
1213 brittle crust. *Earth Planet. Sci. Lett.* 243, 786–804.  
1214 <https://doi.org/10.1016/j.epsl.2006.01.014>

1215 Galland, O., Holohan, E.P., van Wyk de Vries, B., Burchardt, S., 2018. Laboratory Modelling  
1216 of Volcano Plumbing Systems: A Review, in: Breikreuz, C., Rocchi, S. (Eds.), *Physical  
1217 Geology of Shallow Magmatic Systems - Dykes, Sills and Laccoliths*. Springer Berlin  
1218 Heidelberg, pp. 147–214.

1219 Galland, O., Planke, S., Neumann, E.R., Malthe-Sorensen, A., 2009. Experimental modelling  
1220 of shallow magma emplacement: Application to saucer-shaped intrusions. *Earth Planet.  
1221 Sci. Lett.* 277, 373–383. <https://doi.org/10.1016/j.epsl.2008.11.003>

1222 Gibbings, J.C., 2011. *Dimensional analysis*. Springer, London.

1223 Gomes, C.J.S., Caldeira, J.N.M., Freitas, A.R., 2006. The influence of different colours on the  
1224 mechanical behaviour of quartz sand – first results. *Ouro Preto Minas Gerais* 35, 400–0.

1225 Graveleau, F., Malavieille, J., Dominguez, S., 2012. Experimental modelling of orogenic  
1226 wedges: A review. *Tectonophysics* 538–540, 1–66.  
1227 <https://doi.org/10.1016/j.tecto.2012.01.027>

1228 Grosse, P., Poppe, S., Delcamp, A., van Wyk de Vries, B., Kervyn, M., 2020. Volcano growth  
1229 versus deformation by strike-slip faults: Morphometric characterization through  
1230 analogue modelling. *Tectonophysics* 228411.  
1231 <https://doi.org/10.1016/j.tecto.2020.228411>

1232 Herbert, J.W., Cooke, M.L., Souloumiac, P., Madden, E.H., Mary, B.C.L., Maillot, B., 2015.  
1233 The work of fault growth in laboratory sandbox experiments. *Earth Planet. Sci. Lett.* 432,  
1234 95–102. <https://doi.org/10.1016/j.epsl.2015.09.046>

1235 Holland, M., van Gent, H., Bazalgette, L., Yassir, N., Hoogerduijn Strating, E.H., Urai, J.L.,  
1236 2011. Evolution of dilatant fracture networks in a normal fault - Evidence from 4D  
1237 model experiments. *Earth Planet. Sci. Lett.* 304, 399–406.  
1238 <https://doi.org/10.1016/j.epsl.2011.02.017>

1239 Holohan, E.P., Van Wyk de Vries, B., Troll, V.R., 2008. Analogue models of caldera collapse  
1240 in strike-slip tectonic regimes. *Bull. Volcanol.* 70, 773–796.  
1241 <https://doi.org/10.1007/s00445-007-0166-x>

1242 Holohan, E.P., Walter, T.R., Schöpfer, M.P.J., Walsh, J.J., Van Wyk De Vries, B., Troll,

1243 V.R., 2013. Origins of oblique-slip faulting during caldera subsidence. *J. Geophys. Res.*  
1244 *Solid Earth* 118, 1778–1794. <https://doi.org/10.1002/jgrb.50057>

1245 Hubbert, M.K., 1951. Mechanical basis for certain familiar geologic structures. *Bull. Geol.*  
1246 *Soc. Am.* 62, 355–372. [https://doi.org/10.1130/0016-](https://doi.org/10.1130/0016-7606(1951)62[355:MBFCFG]2.0.CO;2)  
1247 [7606\(1951\)62\[355:MBFCFG\]2.0.CO;2](https://doi.org/10.1130/0016-7606(1951)62[355:MBFCFG]2.0.CO;2)

1248 Hubbert, M.K., 1945. Strength of the Earth. *Am. Assoc. Pet. Geol. Bull.* 29, 1630–1653.

1249 Hubbert, M.K., 1937. Theory of scale models as applied to the study of geologic structures.  
1250 *GSA Bull.* 48, 1459–1520.

1251 Jaeger, J.C., Cook, N.G.W., Zimmerman, R.W., 2007. *Fundamentals of Rock Mechanics*,  
1252 Cambridge University Press. <https://doi.org/10.1017/CBO9781107415324.004>

1253 Jansen, H.A., 1895. Versuche über Getreidedruck in Silozellen. *Zeitschrift des Vereiner*  
1254 *Dtsch. Ingenieure* 39, 1045–1049.

1255 Kavanagh, J.L., Burns, A.J., Hilmi Hazim, S., Wood, E.P., Martin, S.A., Hignett, S., Dennis,  
1256 D.J.C., 2018a. Challenging dyke ascent models using novel laboratory experiments:  
1257 Implications for reinterpreting evidence of magma ascent and volcanism. *J. Volcanol.*  
1258 *Geotherm. Res.* 354, 87–101. <https://doi.org/10.1016/j.jvolgeores.2018.01.002>

1259 Kavanagh, J.L., Engwell, S., Martin, S., 2018b. A review of analogue and numerical  
1260 modelling in volcanology. *Solid Earth* 9, 531–571. [https://doi.org/10.5194/se-9-531-](https://doi.org/10.5194/se-9-531-2018)  
1261 [2018](https://doi.org/10.5194/se-9-531-2018)

1262 Kervyn, M., Boone, M.N., de Vries, B. van W., Lebas, E., Cnudde, V., Fontijn, K., Jacobs, P.,  
1263 2010. 3D imaging of volcano gravitational deformation by computerized X-ray micro-  
1264 tomography. *Geosphere* 6, 482–498. <https://doi.org/10.1130/ges00564.1>

1265 Kervyn, M., Ernst, G.G.J., Van Wyk De Vries, B., Mathieu, L., Jacobs, P., 2009. Volcano  
1266 load control on dyke propagation and vent distribution: Insights from analogue  
1267 modeling. *J. Geophys. Res.* 114, 26. <https://doi.org/10.1029/2008JB005653>

1268 Klinkmüller, M., Schreurs, G., Rosenau, M., Kemnitz, H., 2016. Properties of granular  
1269 analogue model materials: A community wide survey. *Tectonophysics* 684, 23–38.  
1270 <https://doi.org/10.1016/j.tecto.2016.01.017>

1271 Krantz, R.W., 1991. Measurements of friction coefficients and cohesion for faulting and fault  
1272 reactivation in laboratory models using sand and sand mixtures. *Tectonophysics* 188,  
1273 203–207. [https://doi.org/10.1016/0040-1951\(91\)90323-K](https://doi.org/10.1016/0040-1951(91)90323-K)

1274 Labuz, J.F., Zeng, F., Makhnenko, R., Li, Y., 2018. Brittle failure of rock: A review and  
1275 general linear criterion. *J. Struct. Geol.* 112, 7–28.  
1276 <https://doi.org/10.1016/j.jsg.2018.04.007>

1277 Lohrmann, J., Kukowski, N., Adam, J., Oncken, O., 2003. The impact of analogue material  
1278 properties on the geometry, kinematics, and dynamics of convergent sand wedges. *J.*  
1279 *Struct. Geol.* 25, 1691–1711. [https://doi.org/10.1016/S0191-8141\(03\)00005-1](https://doi.org/10.1016/S0191-8141(03)00005-1)

1280 Maillot, B., 2013. A sedimentation device to produce uniform sand packs. *Tectonophysics*  
1281 593, 85–94. <https://doi.org/10.1016/j.tecto.2013.02.028>

1282 Mair, K., Frye, K.M., Marone, C., 2002. Influence of grain characteristics on the friction of  
1283 granular shear zones. *J. Geophys. Res. Solid Earth* 107, ECV 4-1-ECV 4-9.  
1284 <https://doi.org/10.1029/2001jb000516>

1285 Marti, J., Ablay, G.J., Redshaw, L.T., Sparks, R.S.J., 1994. Experimental study of collapse  
1286 calderas. *J. Geol. Soc. London.* 151, 919–929.

1287 Mastin, L.G., Pollard, D.D., 1988. Surface deformation and shallow dike intrusion processes  
1288 at Inyo Craters, Long Valley, California. *J. Geophys. Res.* 93, 13221–13235.  
1289 <https://doi.org/10.1029/JB093iB11p13221>

1290 Mathieu, L., van Wyk de Vries, B., Holohan, E.P., Troll, V.R., 2008. Dykes, cups, saucers  
1291 and sills: Analogue experiments on magma intrusion into brittle rocks. *Earth Planet. Sci.*  
1292 *Lett.* 271, 1–13. <https://doi.org/10.1016/j.epsl.2008.02.020>

1293 Merle, O., 2015. The scaling of experiments on volcanic systems. *Front. Earth Sci.* 3, 1–15.  
1294 <https://doi.org/10.3389/feart.2015.00026>

1295 Merle, O., Borgia, A., 1996. Scaled experiments of volcanic spreading. *J. Geophys. Res.* 101,  
1296 13805. <https://doi.org/10.1029/95JB03736>

1297 Merle, O., Lénat, J.-F., 2003. Hybrid collapse mechanism at Piton de la Fournaise volcano,  
1298 Reunion Island, Indian Ocean. *J. Geophys. Res.* 108, 1–11.  
1299 <https://doi.org/10.1029/2002JB002014>

1300 Montanari, D., Agostini, A., Bonini, M., Corti, G., Del Ventisette, C., 2017. The use of  
1301 empirical methods for testing granular materials in analogue modelling. *Materials*  
1302 (Basel). 10, 1–18. <https://doi.org/10.3390/ma10060635>

1303 Moulas, E., Sokoutis, D., Willingshofer, E., 2019. Pressure build-up and stress variations  
1304 within the Earth's crust in the light of analogue models. *Sci. Rep.* 9, 1–8.  
1305 <https://doi.org/10.1038/s41598-018-38256-1>

1306 Mourgues, R., Cobbold, P.R., 2003. Some tectonic consequences of fluid overpressures and  
1307 seepage forces as demonstrated by sandbox modelling. *Tectonophysics* 376, 75–97.  
1308 [https://doi.org/10.1016/S0040-1951\(03\)00348-2](https://doi.org/10.1016/S0040-1951(03)00348-2)

1309 Nieuwland, D.A., Urai, J.L., Knoop, M., 2000. In-situ stress measurements in model  
1310 experiments of tectonic faulting. In: Lehner F.K., Urai J.L. (eds) *Aspects of Tectonic*

1311           Faulting. Springer, Berlin, Heidelberg.

1312 Paguican, E.M.R., van Wyk de Vries, B., Lagmay, A.M.F., 2014. Hummocks: How they form  
1313           and how they evolve in rockslide-debris avalanches. *Landslides* 11, 67–80.  
1314           <https://doi.org/10.1007/s10346-012-0368-y>

1315 Panien, M., Schreurs, G., Pfiffner, A., 2006. Mechanical behaviour of granular materials used  
1316           in analogue modelling: insights from grain characterisation, ring-shear tests and  
1317           analogue experiments. *J. Struct. Geol.* 28, 1710–1724.  
1318           <https://doi.org/10.1016/j.jsg.2006.05.004>

1319 Park, S.H., L. Manzello, S., Bentz, D.P., Mizukami, T., 2010. Determining thermal properties  
1320           of gypsum board at elevated temperatures. *Fire Mater.* 34, 237–250.  
1321           <https://doi.org/10.1002/fam.1017>

1322 Paterson, M.S., Wong, T., 2005. Experimental rock deformation-the brittle field, 2nd ed.  
1323           Springer Science & Business Media.

1324 Poppe, S., Holohan, E.P., Galland, O., Buls, N., Van Gompel, G., Keelson, B., Tournigand,  
1325           P.-Y., Brancart, J., Hollis, D., Nila, A., Kervyn, M., 2019. An Inside Perspective on  
1326           Magma Intrusion: Quantifying 3D Displacement and Strain in Laboratory Experiments  
1327           by Dynamic X-Ray Computed Tomography. *Front. Earth Sci.* 7, 62.  
1328           <https://doi.org/10.3389/feart.2019.00062>

1329 Poppe, S., Holohan, E.P., Pauwels, E., Cnudde, V., Kervyn, M., 2015. Sinkholes, pit craters,  
1330           and small calderas: Analog models of depletion-induced collapse analyzed by computed  
1331           X-ray microtomography. *Bull. Geol. Soc. Am.* 127, 281–296.  
1332           <https://doi.org/10.1130/B30989.1>

1333 Poppe, S., Holohan, E.P., Rudolf, M., Rosenau, M., Galland, O., Delcamp, A., Van Gompel,  
1334           G., Buls, N., Soens, B., Pohlenz, A., Mourgues, R., Kervyn, M., 2021. Mechanical test  
1335           data of quartz sand, garnet sand, gypsum powder (plaster), kaolin and sand-plaster  
1336           mixtures used as granular analogue materials in geoscience laboratory experiments. *GFZ*  
1337           Data Serv. <https://doi.org/https://doi.org/10.5880/fidgeo.2021.005>

1338 Reber, J.E., Cooke, M.L., Dooley, T.P., 2020. What model material to use? A Review on rock  
1339           analogs for structural geology and tectonics. *Earth-Science Rev.* 202, 103107.  
1340           <https://doi.org/10.1016/j.earscirev.2020.103107>

1341 Reid, H.F., 1911. The elastic-rebound theory of earthquakes. *Univ. Calif. Publ. Dep. Geol.*  
1342           Sci.

1343 Rincón, M., Márquez, A., Herrera, R., Alonso-Torres, A., Granja-Bruña, J.L., van Wyk de  
1344           Vries, B., 2018. Contrasting catastrophic eruptions predicted by different intrusion and



1345 collapse scenarios. *Sci. Rep.* 8, 6178. <https://doi.org/10.1038/s41598-018-24623-5>

1346 Ritter, M.C., Leever, K., Rosenau, M., Oncken, O., 2016. Scaling the sandbox—Mechanical  
1347 (dis) similarities of granular materials and brittle rock. *J. Geophys. Res. Solid Earth* 121,  
1348 6863–6879. <https://doi.org/10.1002/2016JB012915>

1349 Ritter, M.C., Rosenau, M., Oncken, O., 2018a. Growing Faults in the Lab: Insights Into the  
1350 Scale Dependence of the Fault Zone Evolution Process. *Tectonics* 37, 140–153.  
1351 <https://doi.org/10.1002/2017TC004787>

1352 Ritter, M.C., Santimano, T., Rosenau, M., Leever, K., Oncken, O., 2018b. Sandbox  
1353 rheometry: Co-evolution of stress and strain in Riedel– and Critical Wedge–experiments.  
1354 *Tectonophysics* 722, 400–409. <https://doi.org/10.1016/j.tecto.2017.11.018>

1355 Rivalta, E., Taisne, B., Bungler, A.P., Katz, R.F., 2015. A review of mechanical models of  
1356 dike propagation: Schools of thought, results and future directions. *Tectonophysics* 638,  
1357 1–42. <https://doi.org/10.1016/j.tecto.2014.10.003>

1358 Roche, O., Druitt, T.H., Merle, O., 2000. Experimental study of caldera formation. *J.*  
1359 *Geophys. Res.* 105, 395. <https://doi.org/10.1029/1999JB900298>

1360 Roche, O., Van Wyk De Vries, B., Druitt, T.H., 2001. Sub-surface structures and collapse  
1361 mechanisms of summit pit craters. *J. Volcanol. Geotherm. Res.* 105, 1–18.  
1362 [https://doi.org/10.1016/S0377-0273\(00\)00248-1](https://doi.org/10.1016/S0377-0273(00)00248-1)

1363 Rosenau, M., Corbi, F., Dominguez, S., 2017. Analogue earthquakes and seismic cycles:  
1364 Experimental modelling across timescales. *Solid Earth* 8, 597–635.  
1365 <https://doi.org/10.5194/se-8-597-2017>

1366 Rosenau, M., Lohrmann, J., Oncken, O., 2009. Shocks in a box: An analogue model of  
1367 subduction earthquake cycles with application to seismotectonic forearc evolution. *J.*  
1368 *Geophys. Res. Solid Earth* 114, 1–20. <https://doi.org/10.1029/2008JB005665>

1369 Rudolf, M., Warsitzka, M., 2019. RST Evaluation - Scripts for analysing shear experiments  
1370 from the Schulze RST.pc01 ring shear tester.

1371 Sarkar, P.K., Mitra, N., 2019. Gypsum under tensile loading: A molecular dynamics study.  
1372 *Constr. Build. Mater.* 201, 1–10. <https://doi.org/10.1016/j.conbuildmat.2018.12.097>

1373 Scheibert, J., Galland, O., Hafver, A., 2017. Inelastic deformation during sill and laccolith  
1374 emplacement: Insights from an analytic elastoplastic model. *J. Geophys. Res. Solid Earth*  
1375 122, 923–945. <https://doi.org/10.1002/2016JB013754>

1376 Schellart, W.P., 2000. Shear test results for cohesion and friction coefficients for different  
1377 granular materials: Scaling implications for their usage in analogue modelling.  
1378 *Tectonophysics* 324, 1–16. [https://doi.org/10.1016/S0040-1951\(00\)00111-6](https://doi.org/10.1016/S0040-1951(00)00111-6)

1379 Schellart, W.P., Strak, V., 2016. A review of analogue modelling of geodynamic processes:  
1380 Approaches, scaling, materials and quantification, with an application to subduction  
1381 experiments. *J. Geodyn.* 100, 7–32. <https://doi.org/10.1016/j.jog.2016.03.009>

1382 Scholz, C.H., 1972. Static fatigue of quartz. *J. Geophys. Res.* 77, 2104–2114.  
1383 <https://doi.org/10.1029/jb077i011p02104>

1384 Schöpfer, M.P.J., Abe, S., Childs, C., Walsh, J.J., 2009. The impact of porosity and crack  
1385 density on the elasticity, strength and friction of cohesive granular materials: Insights  
1386 from DEM modelling. *Int. J. Rock Mech. Min. Sci.* 46, 250–261.  
1387 <https://doi.org/10.1016/j.ijrmms.2008.03.009>

1388 Schöpfer, M.P.J., Childs, C., Manzocchi, T., 2013. Three-dimensional failure envelopes and  
1389 the brittle-ductile transition. *J. Geophys. Res. Solid Earth* 118, 1378–1392.  
1390 <https://doi.org/10.1002/jgrb.50081>

1391 Schreurs, G., Buitter, S.J.H., Boutelier, D., Corti, G., Costa, E., Cruden, a. R., Daniel, J.-M.,  
1392 Hoth, S., Koyi, H. a., Kukowski, N., Lohrmann, J., Ravaglia, a., Schlische, R.W.,  
1393 Withjack, M.O., Yamada, Y., CavoZZi, C., Del Ventisette, C., Brady, J. a. E., Hoffmann-  
1394 Rothe, a., Mengus, J.-M., Montanari, D., Nilfouroushan, F., 2006. Analogue benchmarks  
1395 of shortening and extension experiments. *Geol. Soc. London, Spec. Publ.* 253, 1–27.  
1396 <https://doi.org/10.1144/GSL.SP.2006.253.01.01>

1397 Schreurs, G., Buitter, S.J.H., Boutelier, J., Burberry, C., Callot, J.-P., CavoZZi, C., Cerca, M.,  
1398 Chen, J.-H., Cristallini, E., Cruden, A.R., Cruz, L., Daniel, J.-M., Da Poian, G., Garcia,  
1399 V.H., Gomes, C.J.S., Grall, C., Guillot, Y., Guzmán, C., Hidayah, T.N., Hilley, G.,  
1400 Klinkmüller, M., Koyi, H.A., Lu, C.-Y., Maillot, B., Meriaux, C., Nilfouroushan, F.,  
1401 Pan, C.-C., Pillot, D., Portillo, R., Rosenau, M., Schellart, W.P., Schlische, R.W., Take,  
1402 A., Vendeville, B., Vergnaud, M., Vettori, M., Wang, S.-H., Withjack, M.O., Yagupsky,  
1403 D., Yamada, Y., 2016. Benchmarking analogue models of brittle thrust wedges. *J. Struct.*  
1404 *Geol.* <https://doi.org/10.1016/j.jsg.2016.03.005>

1405 Schreurs, G., Hanni, R., Panien, M., Vock, P., 2003. Analysis of analogue models by helical  
1406 X-ray computed tomography. *Geol. Soc. London, Spec. Publ.* 215, 213–223.  
1407 <https://doi.org/10.1144/GSL.SP.2003.215.01.20>

1408 Schultz, R.A., 1996. Relative scale and the strength and deformability of rock masses. *J.*  
1409 *Struct. Geol.* 18, 1139–1149. [https://doi.org/10.1016/0191-8141\(96\)00045-4](https://doi.org/10.1016/0191-8141(96)00045-4)

1410 Schulze, D., 1994. Entwicklung und Anwendung eines neuartigen Ringschergerätes.  
1411 *Aufbereitungstechnik* 35, 524–535.

1412 Seropian, G., Stix, J., 2018. Monitoring and forecasting fault development at actively forming

1413 calderas: An experimental study. *Geology* 46, 23–26. <https://doi.org/10.1130/G39551.1>

1414 Shea, T., van Wyk de Vries, B., 2008. Structural analysis and analogue modeling of the  
1415 kinematics and dynamics of rockslide avalanches. *Geosphere* 4, 657–686.  
1416 <https://doi.org/10.1130/GES00131.1>

1417 Souloumiac, P., Maillot, B., Leroy, Y.M., 2012. Bias due to side wall friction in sand box  
1418 experiments. *J. Struct. Geol.* 35, 90–101. <https://doi.org/10.1016/j.jsg.2011.11.002>

1419 Tortini, R., Bonali, F.L., Corazzato, C., Carn, S.A., Tibaldi, A., 2014. An innovative  
1420 application of the kinect in earth sciences: Quantifying deformation in analogue  
1421 modelling of volcanoes. *Terra Nov.* 26, 273–281. <https://doi.org/10.1111/ter.12096>

1422 Vachon, R., Hieronymus, C.F., 2017. Effect of host-rock rheology on dyke shape, thickness  
1423 and magma overpressure. *Geophys. J. Int.* 208, 1414–1429.  
1424 <https://doi.org/10.1093/gji/ggw448>

1425 van Gent, H.W., Holland, M., Urai, J.L., Loosveld, R., 2010. Evolution of fault zones in  
1426 carbonates with mechanical stratigraphy - Insights from scale models using layered  
1427 cohesive powder. *J. Struct. Geol.* 32, 1375–1391.  
1428 <https://doi.org/10.1016/j.jsg.2009.05.006>

1429 van Mechelen, J.L.M., 2004. Strength of moist sand controlled by surface tension for tectonic  
1430 analogue modelling. *Tectonophysics* 384, 275–284.  
1431 <https://doi.org/10.1016/j.tecto.2004.04.003>

1432 Van Wyk De Vries, B., Merle, O., 1998. Extension induced by volcanic loading in regional  
1433 strike-slip zones. *Geology*. [https://doi.org/10.1130/0091-](https://doi.org/10.1130/0091-7613(1998)026<0983:EIBVLI>2.3.CO;2)  
1434 [7613\(1998\)026<0983:EIBVLI>2.3.CO;2](https://doi.org/10.1130/0091-7613(1998)026<0983:EIBVLI>2.3.CO;2)

1435 Vimmrová, A., Krejsová, J., Scheinherrová, L., Doleželová, M., Keppert, M., 2020. Changes  
1436 in structure and composition of gypsum paste at elevated temperatures. *J. Therm. Anal.*  
1437 *Calorim.* 142, 19–28. <https://doi.org/10.1007/s10973-020-09528-8>

1438 Voight, B., Elsworth, D., 1997. Failure of volcano slopes. *Géotechnique* 47, 1–31.  
1439 <https://doi.org/10.1680/geot.1997.47.1.1>

1440 Wang, K., 2021. If not brittle: Ductile, plastic, or viscous? *Seismol. Res. Lett.* 92, 1181–1184.  
1441 <https://doi.org/10.1785/0220200242>

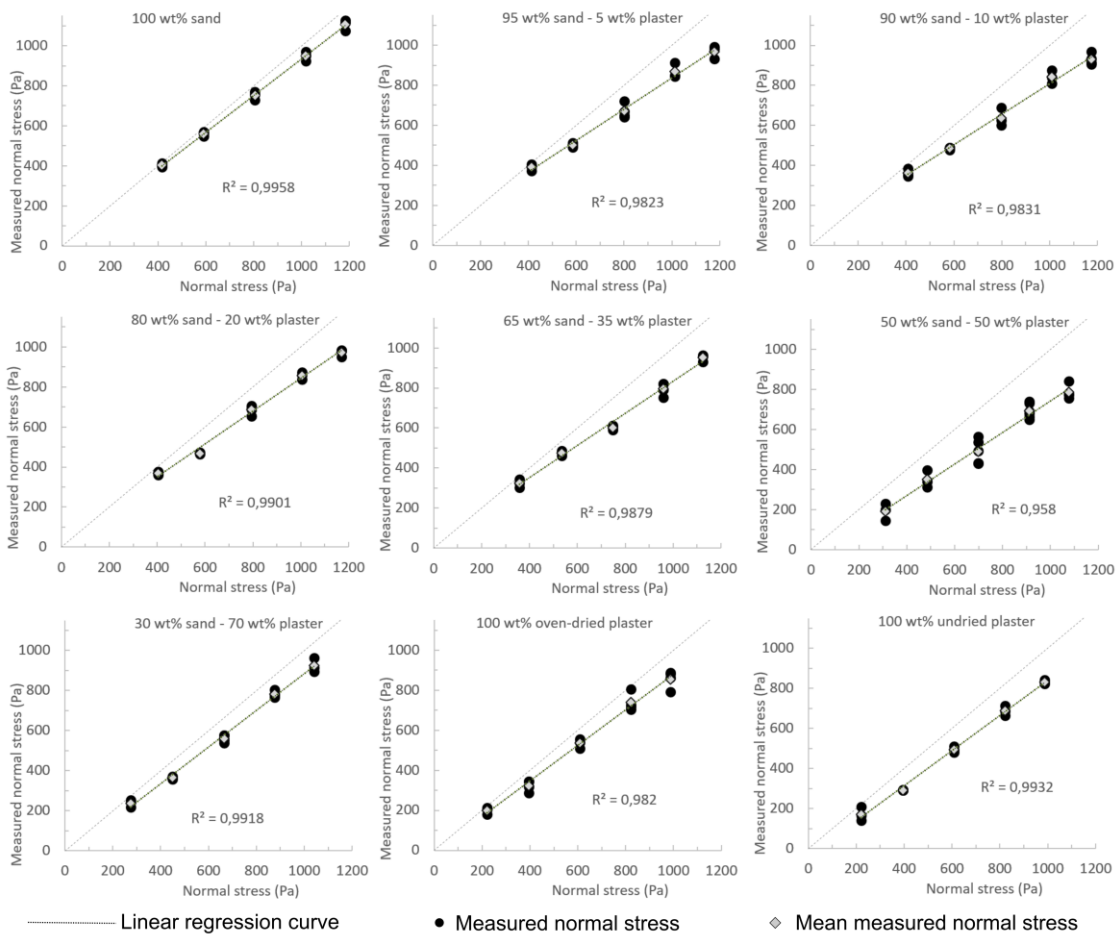
1442 Warsitzka, M., Ge, Z., Schönebeck, J.-M., Pohlenz, A., Kukowski, N., 2019. Ring-shear test  
1443 data of foam glass beads used for analogue experiments in the Helmholtz Laboratory for  
1444 Tectonic Modelling (HelTec) at the GFZ German Research Centre for Geosciences in  
1445 Potsdam and the Institute of Geosciences, Friedrich Schiller University.  
1446 <https://doi.org/10.5880/GFZ.4.1.2019.002>

1447 Williams, S.C., 1988. The shear strength of gypsum single crystals on three cleavage planes.  
1448 Tectonophysics 148, 163–173. [https://doi.org/10.1016/0040-1951\(88\)90168-0](https://doi.org/10.1016/0040-1951(88)90168-0)  
1449 Zorn, E.U., Walter, T.R., Heap, M.J., Kueppers, U., 2020. Insights into lava dome and spine  
1450 extrusion using analogue sandbox experiments. Earth Planet. Sci. Lett. 551, 116571.  
1451 <https://doi.org/10.1016/j.epsl.2020.116571>  
1452 Zwaan, F., Schreurs, G., 2017. How oblique extension and structural inheritance influence rift  
1453 segment interaction: Insights from 4D analog models. Interpretation 5, SD119–SD138.  
1454 <https://doi.org/10.1190/INT-2016-0063.1>  
1455  
1456

1457 **SUPPLEMENTARY MATERIAL**

1458 **Normal load correction of direct shear test data**

1459 Part of the normal stress applied on the horizontal shear plane by the sample and additional  
1460 loads in the upper cylinder is counteracted by friction between the granular sample and the  
1461 plastic of the upper cylinder, also called the ‘silo effect’ or ‘Janssen effect’ (Jansen 1895). The  
1462 method of Mourgues and Cobbold (2003) was used to measure the silo effect empirically, and  
1463 correct the normal loads used to construct the failure envelopes (Figure 8 in main text). The  
1464 upper cylinder was suspended <1 mm above a precision balance, each granular material was  
1465 emplaced and compacted in the same manner as for complete direct shear tests to obtain the  
1466 same densities (Table 2 in main text). The weight then registered by the balance was the  
1467 effective normal load exerted on the failure plane in the direct shear tests. These normal load  
1468 measurements were repeated at least three times for each applied normal load (Figure S1). For  
1469 all materials, these measurements fell on a linear trend with a slope lower than that of the  
1470 zero-friction diagonal line. To ensure reproducibility of the measurements, more runs were  
1471 added if necessary to reach a  $r^2 > 0.990$  linear regression value of the data in a measured  
1472 normal load vs. theoretical normal load (i.e. zero friction between material and cylinder wall)  
1473 plot.



1475

1476 **Figure S1** – Measured normal stress versus theoretical (i.e. zero-friction) normal stress ( $\sigma_n$ ) plots for sand and  
 1477 plaster and their mixtures. The means were used as normal load values in the direct shear test results that  
 1478 reconstruct the failure envelopes of Figure 6.

1479

1480